Available online at www.sciencedirect.com
SCIENCE DIRECT®
Journal of Solid State Chemistry 179 (2006) 2212–2230
JOURNAL OF SOLID STATE CHEMISTRY
www.elsevier.com/locate/jssc

Systems *R*–Fe–O (*R* = Ho, Er): Thermodynamic properties of ternary oxides using differential scanning calorimetry and solid-state electrochemical cells

S.C. Parida*, S.K. Rakshit, S. Dash, Ziley Singh, B.K. Sen, V. Venugopal

Product Development Section, Radiochemistry and Isotope Group, Bhabha Atomic Research Centre, Trombay, Mumbai—400 085, India

Received 15 February 2006; received in revised form 17 April 2006; accepted 29 April 2006
Available online 28 April 2006

Abstract

The thermodynamic properties of three different types of ternary oxides $RFeO_3$(s), $R_3Fe_5O_{12}$(s) and RFe_2O_4(s) (where R = Ho and Er) have been determined by calorimetric and solid-state galvanic cell methods. Heat capacities of $RFeO_3$(s) and $R_3Fe_5O_{12}$(s) have been determined by differential scanning calorimetry from 130 to 860 K. Heat capacity measurements from 130 to 860 K revealed λ-type anomalies for $RFeO_3$(s) and $R_3Fe_5O_{12}$(s) compounds which are assigned due to magnetic order–disorder transitions. The oxygen chemical potentials corresponding to the three-phase equilibria involving these ternary oxides have been determined by using solid-state electrochemical cells. The standard molar Gibbs energies of formation of $RFeO_3$(s), $R_3Fe_5O_{12}$(s) and RFe_2O_4(s) have been computed from the oxygen potential data. Based on the thermodynamic information, oxygen potential diagrams have been computed for the systems *R*–Fe–O (R = Ho and Er) at two different temperatures: T = 1250 and 1450 K. Thermodynamic functions like $C^o_{p,m}$, S^o_m, H^o, G^o, $(H^o_T - H^o_0)$, $(H^o_T - H^o_{298.15\,K})$, $-(G^o_T - H^o_{298.15\,K})/T$, $\Delta_f H^o_m$, and $\Delta_f G^o_m$ have been generated for the compounds $RFeO_3$(s) and $R_3Fe_5O_{12}$(s) based on the experimental data obtained in this study and the available data in the literature.

Keywords: System Ho–Fe–O; System Er–Fe–O; Rare-earth orthoferrites; Rare-earth iron garnets; Heat capacity; Order–disorder transitions; Gibbs energy of formation; Oxygen chemical potential; Solid-state electrochemical technique; Differential scanning calorimetry

1. Introduction

The two important classes of compounds in the systems *R*–Fe–O (where R = rare earth element) are: the rare-earth orthoferrites $RFeO_3$(s) and the rare-earth iron garnets $R_3Fe_5O_{12}$(s). These two types of compounds have potential use in materials science and technology [1–5]. The practical application of these oxides and some of their substituted analogues include high temperature superconductors, magnetic bubble layers for storage devices, electrode materials for solid oxide fuel cells and materials for sensor technology. The physico-chemical properties of these ternary oxides are important for their practical applications. The crystal structures and magnetic properties of these compounds have been thoroughly investigated by many researchers. However, the thermodynamic properties of these oxides have been studied to a limited extent. Quantitative information on the thermodynamic properties of these oxides will enable to predict their stability in different chemical environments.

Katsura et al. [6] have established the phase diagram of the system R_2O_3–Fe_2O_3–Fe at high temperatures and reported the existence of three ternary oxides: $RFeO_3$(s), $R_3Fe_5O_{12}$(s) and RFe_2O_4(s) for R = Ho and Er. It is evident from their study [6] that for the system Ho–Fe–O, the phase $HoFe_2O_4$(s) disappears below 1453 K, whereas for the system Er–Fe–O, the phase $ErFe_2O_4$(s) disappears below 1350 K. Accordingly, there are two different types of phase relations for these systems. The coexisting equilibrium phases below the decomposition temperature of RFe_2O_4(s) are: $\{RFeO_3(s) + R_2O_3(s) + Fe(s)\}$ and $\{R_3Fe_5O_{12}(s) + RFeO_3(s) + Fe_3O_4(s)\}$, whereas the coexisting equilibrium phases above the decomposition

*Corresponding author. Fax: +91 22 2550 5150, +91 22 2550 5152.
E-mail address: sureshp@apsara.barc.ernet.in (S.C. Parida).

0022-4596/$ - see front matter © 2006 Elsevier Inc. All rights reserved.
doi:10.1016/j.jssc.2006.04.024

temperature are: $\{RFeO_3(s)+RFe_2O_4(s)+R_2O_3(s)\}$, $\{R_3Fe_5O_{12}(s)+RFeO_3(s)+Fe_3O_4(s)\}$ and $\{RFe_2O_4(s)+R_2O_3(s)+Fe(s)\}$. Kimizuka et al. [7] have calculated the Gibbs energies of formation of $RFeO_3(s)$, $R_3Fe_5O_{12}(s)$ and $RFe_2O_4(s)$ from the measured equilibrium oxygen partial pressure over the co-existing phases using gas equilibrium technique in the temperature ranges: $1273 \leqslant T/K \leqslant 1423$, $1273 \leqslant T/K \leqslant 1523$ and $1473 \leqslant T/K \leqslant 1523$, for $R = Ho$ and in the temperature ranges: $1273 \leqslant T/K \leqslant 1423$, $1273 \leqslant T/K \leqslant 1373$ and $1373 \leqslant T/K \leqslant 1473$, for $R = Er$, respectively.

The heat capacity of $HoFeO_3(s)$ have been measured by Saito et al. [8] from 50 to 70 K and by Bhattacharjee et al. [9] from 2.8 to 200 K. Heat capacity of $ErFeO_3(s)$ have been measured by Saito et al. [10] from 6 to 300 K. Heat capacity of $Ho_3Fe_5O_{12}(s)$ and $Er_3Fe_5O_{12}(s)$ have been measured by Harris and Meyer [11] from 1.3 to 20.6 K and by Varazashvilli et al. [12] from 300 to 850 K. Heat capacity data for $RFe_2O_4(s)$ compounds are not reported in the literature.

Parida et al. [13–17] and Rakshit et al. [18] have carried out e.m.f. and calorimetric measurements and found out the thermodynamic properties of $RFeO_3(s)$ (for $R = La$, Nd, Sm, Eu, Gd, Tb and Dy) and $R_3Fe_5O_{12}(s)$ (for $R = Sm$, Eu, Gd, Tb and Dy).

In the present study, heat capacity measurements have been carried out for $RFeO_3(s)$ and $R_3Fe_5O_{12}(s)$ ($R = Ho$, Er) from 130 to 860 K using differential scanning calorimetry (DSC). Solid-state electrochemical technique employing oxide-ion conducting electrolytes have been used to measure the oxygen potential over various three-phase coexisting electrodes and the standard molar Gibbs energies of formation of $RFeO_3(s)$, $R_3Fe_5O_{12}(s)$ and $RFe_2O_4(s)$ have been calculated from the measured oxygen potentials. Other thermodynamic quantities have been calculated from the experimental data. The principles of heat capacity measurement by using DSC and oxygen chemical potential measurements using solid-state electrochemical cells have been described in detail in earlier publications [18–20].

2. Experimental

2.1. Materials preparation

The citrate–nitrate gel combustion method was followed for the preparation of $RFeO_3(s)$ and $R_3Fe_5O_{12}(s)$. Preheated $R_2O_3(s)$ (LEICO Industries Inc., USA, 0.999 mass fraction), ferrous ammonium sulphate (Mohr's salt; Qualigens Fine Chemicals, Mumbai, 0.99 mass fraction) were used as the starting materials. The Mohr's salt was dissolved in conc. HNO_3 in order to oxidize Fe^{2+} ions to Fe^{3+} ions and then diluted to ~6 M. Stoichiometric amount of preheated $R_2O_3(s)$ was dissolved in dilute HNO_3. Both the solutions were mixed and excess amount of citric acid (E. Merck, India, 0.995 mass fraction) was added to the solution to assist complete dissolution. The solution was heated on a hot plate at around $T = 375$ K to remove water and oxides of nitrogen. A gel was formed which was heated at $T = 450$ K to dryness. The residue was ground in an agate mortar, made into pellets at a pressure of 100 MPa using a steel die and heated at $T = 1473$ K in air in a platinum crucible for 72 h with two intermediate grindings. The products obtained were identified by X-ray diffraction (XRD) analysis using a DIANO X-ray diffractometer with Cu$K\alpha$ radiation ($\lambda = 1.54178$ Å) using a graphite monochromator and found to be single phases. The XRD patterns of $RFeO_3(s)$ and $R_3Fe_5O_{12}(s)$ for $R = Ho$ and Er are shown in Fig. 1.

Attempts to prepare pure $RFe_2O_4(s)$ failed. However, a phase mixture of $\{RFe_2O_4(s)+R_2O_3(s)+Fe(s)\}$ was prepared by heating a homogeneous mixture of $R_2O_3(s)$, $Fe_2O_3(s)$ and Fe(s) in the molar ratio of (2:1:3) in air in a calcia stabilized zirconia cup at $T = 1573$ K and quenching to room temperature. The excess amount of $R_2O_3(s)$ and Fe(s) were taken to ensure the formation of the desired three-phase mixture. The quenched sample was analyzed by XRD analysis and found to contain the three phases, $RFe_2O_4(s)$, $R_2O_3(s)$ and Fe(s).

Pure phases of $RFeO_3(s)$ and $R_3Fe_5O_{12}(s)$ were made into pellets, sintered in air at 1473 K for 24 h, reground and used for heat capacity measurements. Based on the phase relations, phase mixtures: $\{RFeO_3(s)+R_2O_3(s)+Fe(s)\}$, $\{R_3Fe_5O_{12}(s)+RFeO_3(s)+Fe_3O_4(s)\}$, $\{RFe_2O_4(s)+R_2O_3(s)+Fe(s)\}$ and $\{Ni(s)+NiO(s)\}$ were pelletised using a steel die at a pressure of 100 MPa for the e.m.f measurements. The pellets were sintered in purified argon gas atmosphere ($p(O_2) \cong 10^{-13}$ Pa) at $T = 1000$ K for 72 h. The argon gas was purified by passing it through towers containing the reduced form of BASF catalyst, molecular sieves, anhydrous magnesium perchlorate, and hot uranium metal at $T = 550$ K. The oxygen partial pressure in the purified argon gas was calculated from the measured e.m.f. of the cell: (−) Pt/{Ar(g), $p(O_2) = x$ Pa}//CSZ//O_2(g), 101 325 Pa/Pt (+). The calculated value of x is ($p(O_2) \cong 10^{-13}$ Pa) at $T = 1000$ K. The sintered pellets were re-examined by XRD method and the phase compositions were found unchanged.

2.2. Differential scanning calorimetric measurements

The heat flux DSC (Model: DSC 131) supplied by M/s. SETARAM Instrumentations, France, was used to measure the heat capacities of all the samples. The transducer of DSC 131 has been designed using the technology of the plate-shaped DSC rods made of chromel-constantan. It is arranged in a small furnace with a metal resistor of low-thermal inertia so as to produce high heating and cooling rates, thereby providing for high-speed experiments. The transducer also possesses very good sensitivity over the whole temperature range (100–950 K). The temperature calibration of the calorimeter was carried out in the present study by the phase transition temperatures of NIST (National Institute of Standards and

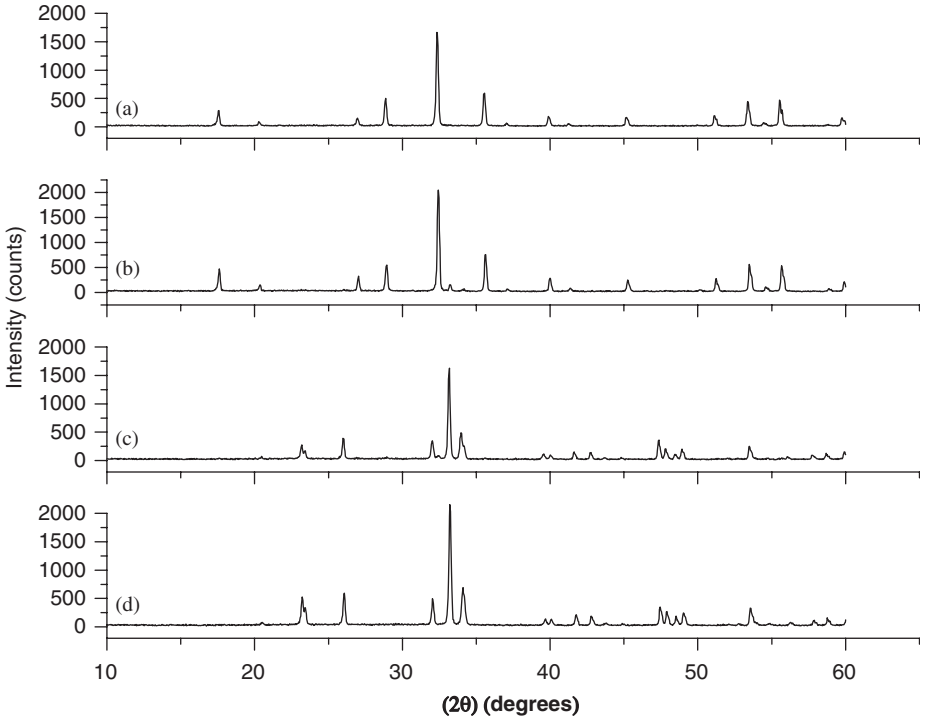

Fig. 1. Powder X-ray diffraction patterns of RFeO$_3$(s) and R_3Fe$_5$O$_{12}$(s): (a) HoFeO$_3$(s); (b) ErFeO$_3$(s); (c) Ho$_3$Fe$_5$O$_{12}$(s) and (d) Er$_3$Fe$_5$O$_{12}$(s).

Technology) reference materials (mercury: $T_{fus} = 234.316\,K$; gallium: $T_{fus} = 302.914\,K$; indium: $T_{fus} = 429.748\,K$; tin: $T_{fus} = 505.078\,K$; lead: $T_{fus} = 600.600\,K$) and AR grade samples (n-pentane: $T_{fus} = 140.490\,K$; cyclohexane: $T_{trs} = 190.0\,K$; $T_{fus} = 280.1\,K$; deionised water: $T_{fus} = 273.160\,K$, potassium nitrate: $T_{trs} = 400.850\,K$; silver sulfate: $T_{trs} = 703.150\,K$; potassium sulfate: $T_{trs} = 856.150\,K$). Heat calibration of the calorimeter was carried out by using the enthalpies of transition of the above-mentioned materials. For the determination of heat capacity, NIST synthetic sapphire (SRM 720) in the powder form was used as the reference material. Heat capacity of all the oxides were determined by the Classical three-step method in the continuous heating mode in two different temperature ranges: (i) $130 \leqslant T/K \leqslant 320$ and (ii) $300 \leqslant T/K \leqslant 860$. Heat flow as a function of temperature was measured in the first temperature range at a heating rate of $5\,K\,min^{-1}$ with high purity helium as a carrier gas with a flow rate of $2\,dm^3\,h^{-1}$. For the second temperature range, high purity argon was used as a carrier gas with the same flow rate as that of helium and same heating rate. Two flat bottom aluminum crucibles of identical masses of capacity $10^{-4}\,dm^3$ with covering lids were used as containers for sample and reference materials. About 300–350 mg of the sample was used for the heat capacity measurements. The accuracy and reproducibility of measurements were checked by measuring the heat capacities of Fe_2O_3 (mass fraction 0.998) and NiO (mass fraction 0.999) and found to be within $\pm 1.5\%$ of the literature values.

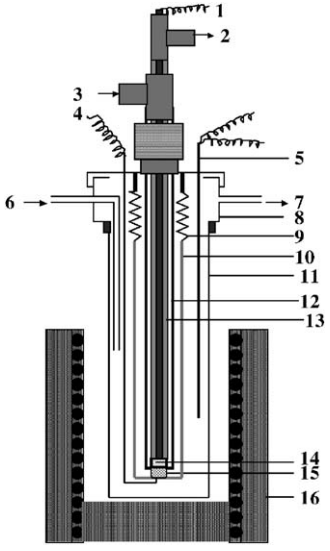

Fig. 2. Schematic diagram of solid-oxide galvanic cell for e.m.f. measurements. (1, 4) Pt-lead wire; (3, 6) gas inlet; (2, 7) gas outlet; (5) thermocouple; (8) stainless steel flange; (9) spring; (10) quartz/alumina holder; (11) quartz/alumina outer tube; (12) CSZ/YSZ electrolyte tube; (13) alumina pressing tube; (14) sample electrode; (15) reference electrode; and (16) Kanthal wire wound/silicon carbide resistance furnace.

2.3. Solid-state electrochemical measurements

Two different types of experimental cell assemblies were used for the e.m.f. measurements: one for measurements up to $T = 1300\,K$ and the other for measurements above this

temperature. The low temperature cell described in Fig. 2 was a double compartment assembly in which the inner compartment was separated from the outer compartment by the use of electrolyte tube. The electrolyte tube separated the gas phase over the two electrodes so that transport of oxygen from the higher oxygen potential electrode to the lower oxygen potential electrode via the gas phase is prevented. The calcia stabilized zirconia (CSZ) electrolyte tube with 15 mol% CaO was supplied by Nikatto Corporation, Japan. The dimensions of the CSZ electrolyte tube were; 13 mm o.d., 9 mm i.d., and 380 mm long with one end closed flat. It has been reported by Pratt [21] that the range of permissible oxygen partial pressures for purely ionic conduction for CSZ electrolyte is about 10^{-20} Pa at $T = 1000$ K and 10^{-13} Pa at $T = 1273$ K. The yttria stabilized zirconia (YSZ) electrolyte has similar range of oxygen partial pressure and temperature for purely ionic conduction. However, for a typical 7.5 mol% yttria doped thoria (YDT) electrolyte, measurements may normally be made down to oxygen partial pressure of 10^{-32} Pa at $T = 1000$ K and 10^{-25} Pa at $T = 1273$ K [21]. An alternative procedure for extending the measurement range to low oxygen partial pressures has been discussed by Shores and Rapp [22]. According to their experiment [22], a bielectrolyte cell involving the solid electrolyte combination of YDT/CSZ can extend the electrolytic conduction domain over that of the single CSZ electrolyte. It has been estimated in the present study that the oxygen partial pressure prevailing over the three-phase mixture $\{R\mathrm{FeO_3(s)} + R_2\mathrm{O_3(s)} + \mathrm{Fe(s)}\}$ is about 10^{-17} Pa at $T = 1000$ K whereas that for the three-phase mixture $\{R_3\mathrm{Fe_5O_{12}(s)} + R\mathrm{FeO_3(s)} + \mathrm{Fe_3O_4(s)}\}$ is about 10^{-15} Pa at $T = 1000$ K. It is evident from the present estimation that the oxygen partial pressure over the phase mixture $\{R\mathrm{FeO_3(s)} + R_2\mathrm{O_3(s)} + \mathrm{Fe(s)}\}$ is near the boundary of the purely ionic conduction domain for CSZ or YSZ electrolyte. It is unwise to use either CSZ or YSZ electrolyte for the measurement of oxygen chemical potential over this phase mixture. Hence, in the present study a bi-electrolyte cell assembly involving the electrolyte combination of YDT/CSZ has been used. The bi-electrolyte cell was arranged in such a way that the YDT electrolyte (in the form of a disc) was adjacent to the electrode having low oxygen chemical potential. This ensured that the transport number of oxygen ion was close to unity for the solid electrolyte combination [22]. An inert environment was maintained over the solid electrodes throughout the experiment by streams of purified argon gas. The argon gas was purified by passing it through towers containing the reduced form of BASF catalyst, molecular sieves, anhydrous magnesium perchlorate and hot uranium metal at $T = 550$ K. The cell temperature (± 1 K) was measured by a calibrated chromel/alumel thermocouple (ITS-90).

The high temperature cell (used above 1300 K) was similar to the low temperature cell with few modifications. The outer quartz jacket was replaced by alumina tube that was forced air cooled near the flange joint. The Kanthal-wire wound furnace was replaced by a (Pt–30%Rh) alloy wire wound resistance furnace. The reference electrode (label 15 in Fig. 2) used was air in all measurements at high temperatures. The measuring electrode was kept inside the electrolyte tube over the YDT disc with a provision to pass high purity inert gas. The temperature of the cell was measured by a calibrated B-type thermocouple (± 1 K).

In both the cases, the e.m.f. (± 0.02 mV) was measured by a Keithely 236 Source Measure Unit (impedance $> 10^{14}$ ohms). E.m.f. measurements were carried out in the temperature range $1050 \leqslant T/\mathrm{K} \leqslant 1250$ with the low temperature cell assembly and in the range $1300 \leqslant T/\mathrm{K} \leqslant 1560$ with the high temperature cell assembly. The reversible e.m.f. of the following solid-state galvanic cells were measured as a function of temperature.

$$\text{Cell (I)}: \ (-)\mathrm{Pt}/\{R\mathrm{FeO_3(s)} + R_2\mathrm{O_3(s)} + \mathrm{Fe(s)}\} \ //\mathrm{YDT}/\mathrm{CSZ}//\{\mathrm{Ni(s)} + \mathrm{NiO(s)}\}/\mathrm{Pt}(+)$$

$$\text{Cell (II)}: \ (-)\mathrm{Pt}/\{R_3\mathrm{Fe_5O_{12}(s)} + R\mathrm{FeO_3(s)} + \mathrm{Fe_3O_4(s)}\}// \ \mathrm{YDT}/\mathrm{CSZ}//\{\mathrm{Ni(s)} + \mathrm{NiO(s)}\}/\mathrm{Pt}(+)$$

$$\text{Cell (III)}: \ (-)\mathrm{Pt}/\{R\mathrm{Fe_2O_4(s)} + R_2\mathrm{O_3(s)} + \mathrm{Fe(s)}\}// \ \mathrm{YDT}/\mathrm{CSZ}//\{\text{air}, \ p(\mathrm{O_2}) = 21.12\,\mathrm{kPa}\}/\mathrm{Pt}(+)$$

The reversibility of the solid-state electrochemical cells was checked by micro-coulometric titration in both directions. A small quantity of current was passed (~ 100 μA for ~ 10 min) through the cell in either direction. After removal of the current source, the cell e.m.f. returned to its original value. The e.m.f. of cells was also found to be independent of flow rate of the inert gas passing over the electrodes in the range from 2×10^{-3} dm^3 min^{-1} to 6×10^{-3} dm^3 min^{-1}. The XRD patterns of the pellets before and after these experiments were found unchanged.

3. Results and discussion

3.1. Heat capacity measurements on $RFeO_3(s)$

The heat capacity data for $\mathrm{HoFeO_3(s)}$ and $\mathrm{ErFeO_3(s)}$ obtained in the present study in the temperature range from 130 to 860 K are combined with the low temperature literature values [8–10] and smoothened using the spline fitting procedure. The smooth values of $C^{\circ}_{\mathrm{p,m}}$ for $\mathrm{HoFeO_3(s)}$ and $\mathrm{ErFeO_3(s)}$ are given in Table 1 and shown in Figs. 3 and 4, respectively.

Heat capacity anomalies have been observed for both $\mathrm{HoFeO_3(s)}$ and $\mathrm{ErFeO_3(s)}$ at 644 and 642 K, respectively, resembling the λ-type transition. From the earlier studies on the orthoferrites [14,15,17,23], it has been observed that the phase transition is second order in nature and involves magnetic order–disorder transition from antiferromagnetic (AF) to paramagnetic state characterized by the Néel temperature (T_{N}). The Néel temperatures reported in the literature [23] from high-temperature Mössbauer measurements are 647 and 645 K for $\mathrm{HoFeO_3(s)}$ and $\mathrm{ErFeO_3(s)}$,

Table 1
Smoothed values of $C^{o}_{p,m}$ of $RFeO_3$(s) (R = Ho and Er) at different temperatures

$HoFeO_3$(s)				$ErFeO_3$(s)			
T/K	$C^{o}_{p,m}$/J K^{-1} mol^{-1}	T/K	$C^{o}_{p,m}$/J K^{-1} mol^{-1}	T/K	$C^{o}_{p,m}$/J K^{-1} mol^{-1}	T/K	$C^{o}_{p,m}$/J K^{-1} mol^{-1}
0	0	425	124.881	0	0	425	124.357
5	2.636	450	127.248	5	1.926	450	125.695
10	1.770	475	129.020	10	1.407	475	126.363
15	1.770	500	130.261	15	3.407	500	127.621
20	3.246	525	131.165	20	5.481	525	129.312
25	7.008	550	132.094	25	7.704	550	131.120
30	9.221	575	133.585	30	10.519	575	133.415
35	13.279	600	136.442	35	13.235	600	135.871
40	16.082	625	141.743	40	15.950	625	139.818
45	19.287	630	143.251	45	18.340	630	141.019
50	22.607	635	144.888	50	21.210	631	141.386
55	26.189	636	145.246	55	23.756	632	141.701
60	28.402	637	145.612	60	26.500	633	141.967
65	30.865	638	145.933	65	29.102	634	142.268
70	33.566	639	146.314	70	31.630	635	142.597
75	36.789	640	146.706	75	34.211	636	142.940
80	38.896	641	147.103	80	36.770	637	143.307
85	41.111	642	147.508	85	39.289	638	143.707
90	44.023	643	147.921	90	41.870	639	144.013
95	46.231	644	144.940	95	44.189	640	144.508
100	48.465	645	144.091	100	46.700	641	144.983
110	52.526	646	142.351	110	51.510	642	145.154
120	57.446	647	140.596	120	56.327	643	144.500
130	60.996	648	139.263	130	61.362	644	142.937
140	65.648	649	138.175	140	65.967	645	141.280
150	70.137	650	137.457	150	70.324	646	139.974
170	77.975	651	136.828	170	78.187	647	138.995
190	84.648	652	136.336	190	84.746	648	138.253
210	90.423	653	135.997	210	90.568	649	137.558
230	95.334	654	135.672	230	95.495	650	137.089
250	99.199	655	135.237	250	99.966	655	135.366
270	102.475	675	132.247	270	103.845	675	132.879
290	105.360	700	131.635	290	107.270	700	131.733
298.15	106.428	725	131.539	298.15	109.306	725	131.094
300	106.696	750	132.731	300	109.512	750	131.365
325	110.382	775	133.802	325	114.765	775	131.689
350	114.178	800	133.421	350	118.715	800	132.115
375	118.054	825	134.253	375	121.652	825	132.467
400	121.991	850	135.028	400	123.179	850	132.642

respectively, which are in close agreement with the values obtained in this study.

The lattice heat capacities of $RFeO_3$(s) are calculated by the approximation of Stølen et al. [24] according to which the lattice contribution can be obtained by adding the lattice contributions of the component oxides. The lattice contributions to the heat capacity of the component oxides R_2O_3(s) and Fe_2O_3(s) are taken from the literature [25–28]. This approximation has been tested for the estimation of lattice heat capacities of $NdGaO_3$(s) $LaAlO_3$(s) and is found to be in good agreement with the experimental values [29]. The lattice heat capacity of $HoFeO_3$(s) and $ErFeO_3$(s) calculated in this way are shown in Figs. 3 and 4, respectively. Earlier literature [8–10] on the low temperature heat capacity measurements on $HoFeO_3$(s) and $ErFeO_3$(s) have shown that the Schottky contribution is absent in these compounds. The magnetic contributions to the heat capacities of $RFeO_3$(s) are calculated by using the relation:

$$C_{\text{magnetic}}(R\text{FeO}_3) = C^{o}_{p,m}R\text{FeO}_3 - 1/2[C_{\text{lattice}}(\text{Fe}_2\text{O}_3) + C_{\text{lattice}}(R_2\text{O}_3) + C_{\text{dilational}}(\text{Fe}_2\text{O}_3) + C_{\text{dilational}}(\text{La}_2\text{O}_3)]. \quad (1)$$

The dilational heat capacity of Fe_2O_3(s) has been taken from literature [28] whereas that for R_2O_3(s) is neglected because of the non-availability of experimental data. However, this will cause a maximum error of $\pm 1\%$, which is well within the uncertainty limit of our estimation method. The magnetic heat capacities for $RFeO_3$(s) calculated in this way are shown in Figs. 3 and 4. The magnetic entropies associated with order–disorder transformation are calculated by integrating the plot of (C_{magnetic}/T) against T in the entire temperature from 0

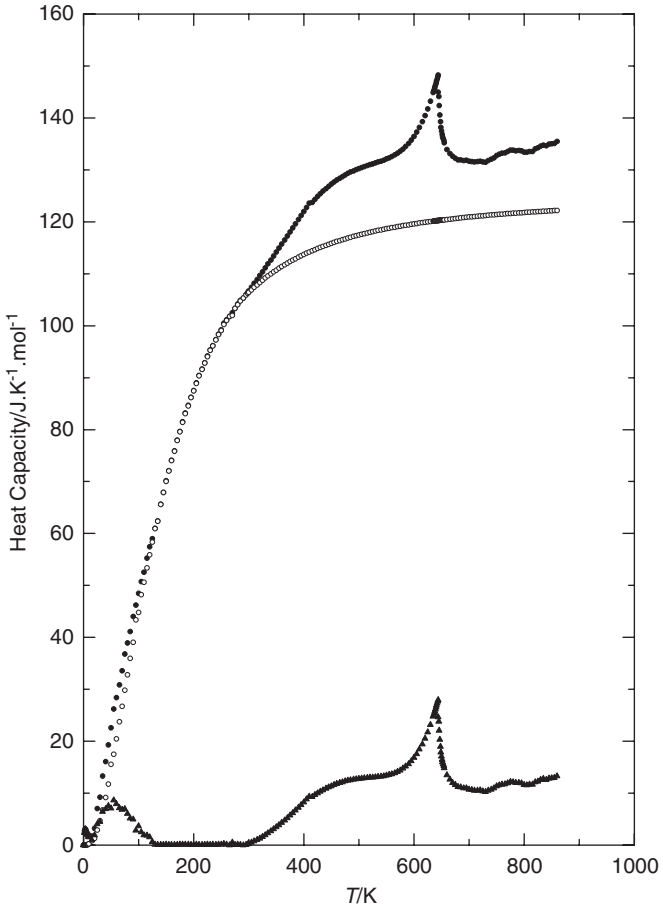

Fig. 3. Plot of heat capacity against temperature for $HoFeO_3$(s) showing different contributions: (●) total heat capacity; (○) lattice contribution; and (▲) magnetic contribution.

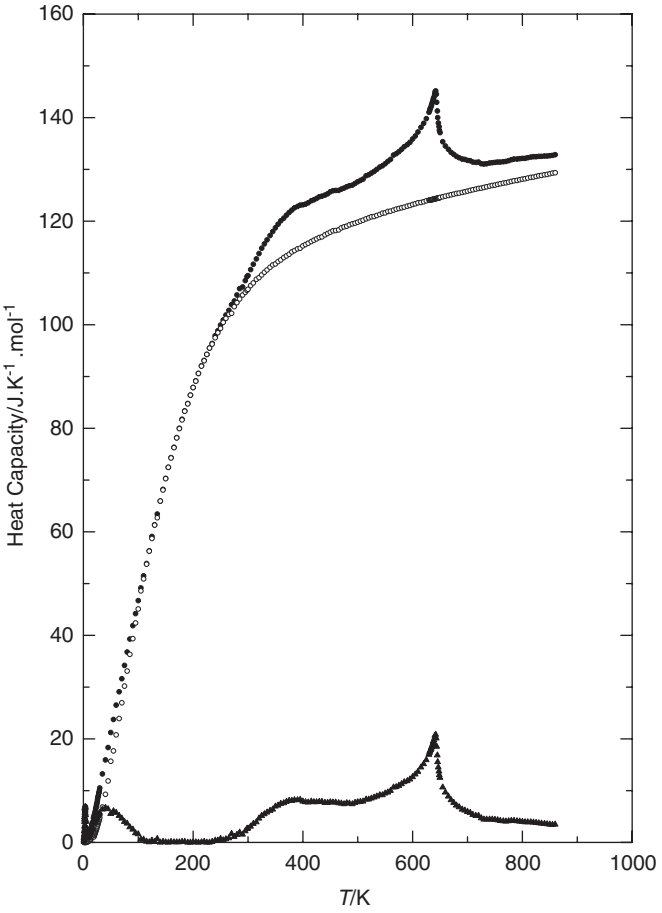

Fig. 4. Plot of heat capacity against temperature for $ErFeO_3$(s) showing different contributions: (●) total heat capacity; (○) lattice contribution; and (▲) magnetic contribution.

to 850 K. The total magnetic entropies calculated for $HoFeO_3$(s) and $ErFeO_3$(s) are equal to 25.9 and 23.8 $J\,K^{-1}\,mol^{-1}$, respectively. The theoretical value of excess magnetic entropy contribution due to delocalization of five unpaired electrons of high spin Fe^{3+} ion is equal to 14.897 $J\,K^{-1}\,mol^{-1}$, according the formula: $S^0_{magnetic} = nR\ln(2S+1)$ (where n = number of Fe-ions, R = universal gas constant, S = total spin quantum number $= \frac{5}{2}$ for Fe^{3+}). The higher values estimated in this study are accounted for the excess contributions arising due to very low temperature ordering of R^{3+} ion.

3.2. Heat capacity measurements on $R_3Fe_5O_{12}$(s)

The heat capacity data obtained in the present study are combined with the literature data and smoothened using the spline fitting procedure in order to get $C^o_{p,m}$ values from 0 to 850 K. The smooth values of $C^o_{p,m}$ for $Ho_3Fe_5O_{12}$(s) and $Er_3Fe_5O_{12}$(s) are listed in Table 2 and shown in Figs. 5 and 6, respectively.

Heat capacity anomalies have been observed for both $Ho_3Fe_5O_{12}$(s) and $Er_3Fe_5O_{12}$(s) at 554 and 544 K, respectively, resembling the λ-type transition. From the earlier studies on the rare-earth iron garnets (RIGs) [12,15,17,30], it has been observed that the phase transition is second order in nature and involves magnetic order–disorder transition from ferromagnetic to paramagnetic state characterized by the Curie temperature (T_C). The Curie temperatures reported in the literature from magnetic measurements are in the vicinity of 550 K, which are in close agreement with the values obtained in this study.

Harris and Meyer [11] have measured the low temperature heat capacities of $R_3Fe_5O_{12}$(s) (R = Sm, Gd, Tb, Dy, Ho, Er, Yb and Lu) from 1.3 to 20.6 K and calculated the Schottky levels of these compounds from the heat capacity data. Henderson et al. [31] have measured the heat capacities of RIGs for R = Eu, Tm, Sm and Yb from 0.4 to 4.2 K and deduced the Debye temperatures of these compounds at 0 K. Varazashvilli et al. [12] have measured the heat capacities of RIGs for R = Sm, Eu, Gd, Tb, Dy and Er from 300 to 850 K. Mirianashvilli et al. [32] have measured the heat capacity of $Lu_3Fe_5O_{12}$(s) from 300 to 900 K. Varazashvilli et al. [33] have measured the low temperature heat capacities of $Gd_3Fe_5O_{12}$(s) and $Lu_3Fe_5O_{12}$(s) from 20 to 300 K. Moretti and Ottonello [34] have calculated the Schottky levels and tabulated the

Table 2
Smoothed values of $C^{o}_{p,m}$ for $R_3Fe_5O_{12}$(s) (R = Ho and Er) at different temperatures

$Ho_3Fe_5O_{12}$(s)				$Er_3Fe_5O_{12}$(s)			
T/K	$C^{o}_{p,m}$/J K^{-1} mol^{-1}	T/K	$C^{o}_{p,m}$/J K^{-1} mol^{-1}	T/K	$C^{o}_{p,m}$/J K^{-1} mol^{-1}	T/K	$C^{o}_{p,m}$/J K^{-1} mol^{-1}
0	0	425	518.3	0	0	425	508.2
5	0.7	450	526.9	5	3.0	450	517.9
10	7.0	475	535.8	10	14.8	475	528.1
15	15.7	500	546.7	15	22.8	500	539.9
20	26.2	525	562.2	20	30.8	525	556.8
25	35.0	530	566.0	25	33.4	530	560.8
30	43.4	535	570.9	30	40.2	535	565.5
35	51.8	540	576.6	35	47.2	540	571.0
40	60.2	541	578.2	40	54.2	541	572.1
45	68.5	542	579.5	45	61.3	542	573.3
50	76.8	543	581.3	50	68.5	543	574.4
55	85.1	544	583.0	55	75.7	544	575.8
60	93.4	545	584.5	60	83.1	545	574.2
65	101.6	546	585.9	65	90.5	546	573.1
70	109.7	547	585.4	70	97.9	547	571.1
75	117.6	548	583.5	75	105.4	548	568.3
80	125.6	549	580.5	80	113.0	549	565.1
85	133.7	550	576.9	85	120.6	550	562.1
90	141.7	555	560.4	90	128.2	555	549.4
95	149.8	560	551.7	95	135.8	560	543.4
100	157.9	565	547.4	100	143.5	565	540.2
110	173.7	570	544.9	110	158.8	570	538.5
120	189.2	575	542.7	120	174.2	575	536.6
130	201.4	600	537.0	130	192.8	600	531.7
140	224.7	625	537.9	140	212.4	625	532.1
150	241.3	650	539.5	150	231.9	650	532.7
170	275.5	675	542.5	170	265.5	675	534.6
190	304.6	700	545.6	190	296.5	700	537.1
210	333.3	725	547.8	210	323.0	725	537.7
230	354.2	750	548.7	230	347.2	750	538.4
250	379.7	775	550.1	250	373.7	775	540.5
270	405.8	800	550.9	270	397.6	800	542.3
290	430.1	825	552.6	290	418.2	825	543.2
298.15	440.8	850	554.2	298.15	427.0	850	544.8
300	443.2			300	430.1		
325	470.6			325	448.4		
350	490.6			350	467.5		
375	499.8			375	484.6		
400	507.6			400	497.7		

thermodynamic functions of all the RIGs based on the available literature data. Parida et al. [15,17] have measured the enthalpy increments of $Sm_3Fe_5O_{12}$(s) and $Dy_3Fe_5O_{12}$(s) from 300 to 1000 K and derived the heat capacities. The lattice contributions to heat capacities for $R_3Fe_5O_{12}$(s) (for R = Ho and Er) are calculated by the procedure similar to $RFeO_3$(s).

Earlier measurements on the low temperature heat capacity of these compounds show substantial Schottky contributions. As explained by Moretti and Ottonello [34], RIGs reveal Schottky anomalies associated with magnetic ordering of paramagnetic Fe^{3+} ions which have unpaired electrons. All possible quantum states $(2S+1)$ and $(2J+1)$ are energetically degenerate and as a first approximation, equally populated as long as the energy differences between the several states are small compared to the thermal energy k_BT (k_B being the Boltzmann constant). At sufficiently low temperatures, k_BT attains the magnitude of the energy gaps, so that the states with lower energies are selectively populated, giving rise to heat capacity anomaly. For the case of $RFeO_3$(s), the magnetic ordering between the R^{3+} and Fe^{3+} ions is not significant to show Schottky anomaly. However, the ordering between R^{3+} at different crystallographic sites is very strong which results in λ-type anomaly in the heat capacity plots of $RFeO_3$(s).

The Schottky contribution to heat capacities for $R_3Fe_5O_{12}$(s) is calculated by taking the energy levels given by Moretti and Ottonello [34]. The dilational contribution is found to be negligible and hence not included in the calculation. The magnetic contribution to heat capacity is found out by subtracting all other contribution from the measured $C^{o}_{p,m}$. The values of magnetic entropies ($S^{o}_{magnetic}$)

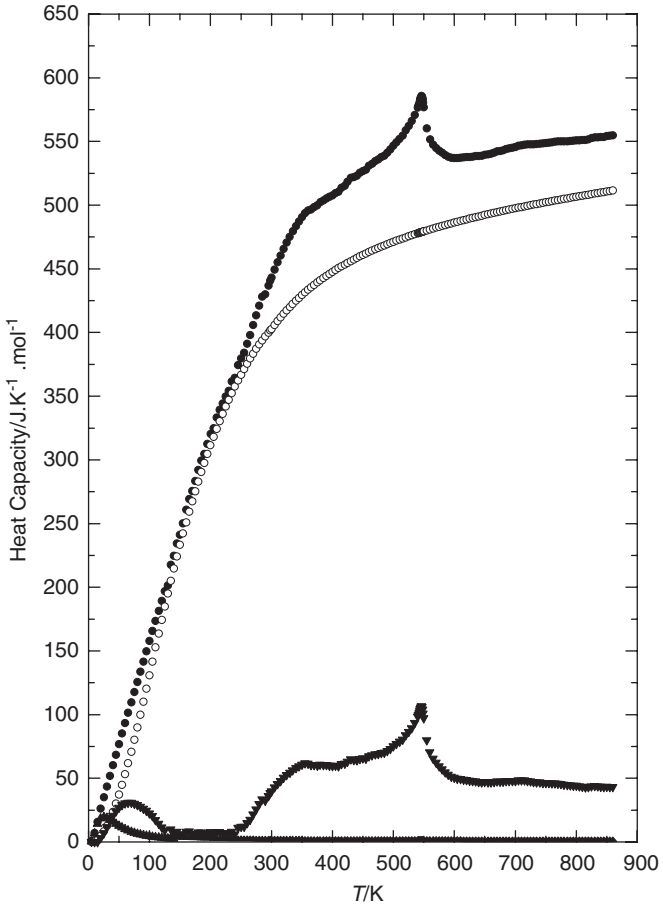

Fig. 5. Plot of heat capacity against temperature for $Ho_3Fe_5O_{12}$(s) showing different contributions: (●) total heat capacity; (○) lattice contribution; (▲) magnetic contribution; and (▼) Schottky contribution.

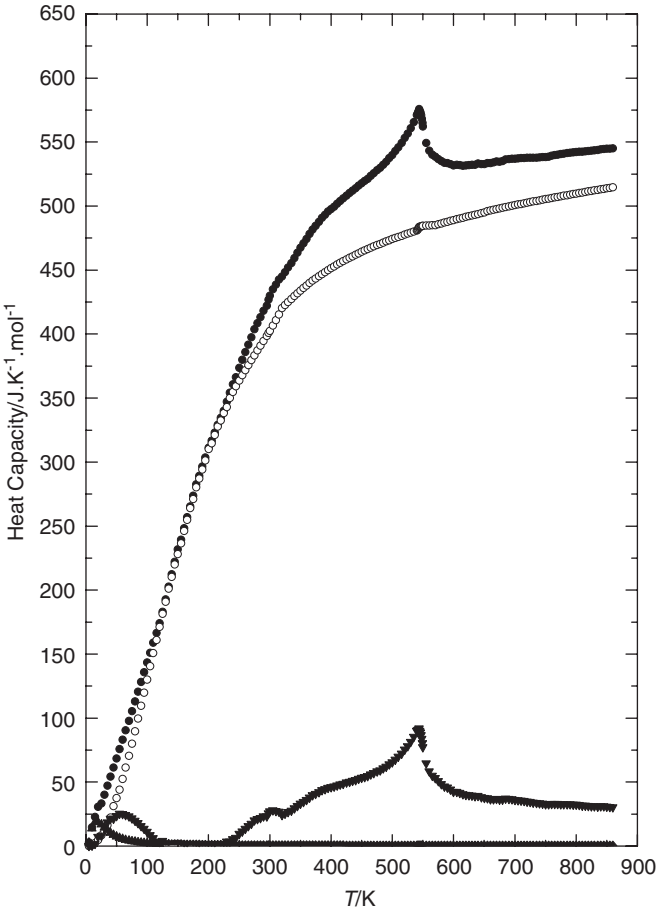

Fig. 6. Plot of heat capacity against temperature for $Er_3Fe_5O_{12}$(s) showing different contributions: (●) total heat capacity; (○) lattice contribution; (▲) magnetic contribution; and (▼) Schottky contribution.

obtained in the present study are: 107.8 and 82.7 $J\,K^{-1}\,mol^{-1}$ for $Ho_3Fe_5O_{12}$(s) and $Er_3Fe_5O_{12}$(s), respectively.

3.3. Oxygen chemical potential over the three-phase electrode {$RFeO_3$(s)+Ho_2O_3(s)+Fe(s)}

The reversible e.m.f.s of the following cell have been measured as a function of temperature.

$$\text{Cell (I)}: \ (-)\text{Pt}/\{R\text{FeO}_3(\text{s}) + R_2\text{O}_3(\text{s}) + \text{Fe(s)}\} \ //\text{YDT}/\text{CSZ}//\{\text{Ni(s)} + \text{NiO(s)}\}/\text{Pt}(+).$$

The variation of e.m.f. for cell (I) with R = Ho and Er as a function of temperature are shown in Fig. 7. The e.m.f. data were least-squares fitted to give the relations:

$$E/\text{V}\ (\pm 0.0002) = 0.2471 + 5.014 \times 10^{-5}\,(T/\text{K}) \quad (1014 \leqslant T/\text{K} \leqslant 1166)\ (\text{for } R = \text{Ho}), \tag{2}$$

$$E/\text{V}\ (\pm 0.0002) = 0.3515 - 2.5318 \times 10^{-5}\,(T/\text{K}) \quad (1099 \leqslant T/\text{K} \leqslant 1231)\ (\text{for } R = \text{Er}). \tag{3}$$

The oxygen chemical potential corresponding to three-phase mixtures: {RFeO$_3$(s) + R_2O$_3$(s) + Fe(s)} in cell (I) has been calculated using Eqs. (2) and (3) and the values of oxygen chemical potential for the phase mixture {Ni(s) + NiO(s)} from Barin [35]. For the equilibrium reaction:

$$2/3\ R_2\text{O}_3(\text{s}) + 4/3\ \text{Fe(s)} + \text{O}_2(\text{g}) = 4/3\ R\text{FeO}_3(\text{s}), \tag{4}$$

the results obtained can be represented by the following expressions:

$$\{\Delta\mu(\text{O}_2)/\text{kJ mol}^{-1}\} \pm 0.5 = -558.9 + 0.1471\,(T/\text{K}) \quad (1014 \leqslant T/\text{K} \leqslant 1166)\ (\text{for } R = \text{Ho}), \tag{5}$$

$$\{\Delta\mu(\text{O}_2)/\text{kJ mol}^{-1}\} \pm 0.5 = -599.2 + 0.1762\,(T/\text{K}) \quad (1099 \leqslant T/\text{K} \leqslant 1231)\ (\text{for } R = \text{Er}). \tag{6}$$

Kimizuka et al. [7] have reported the equilibrium oxygen chemical potential for reaction (4) in the temperature range from 1273 to 1423 K. The values of $\Delta\mu(O_2)$ obtained in the present study are compared with those obtained by Kimizuka et al. [7] in Fig. 8. It is apparent that the results obtained in this study when extrapolated to higher temperatures are in good agreement with those reported by Kimizuka et al. [7] in the whole temperature range from 1014 to 1423 K for R = Ho and in the temperature range from 1099 to 1273 K for R = Er. It has been decided

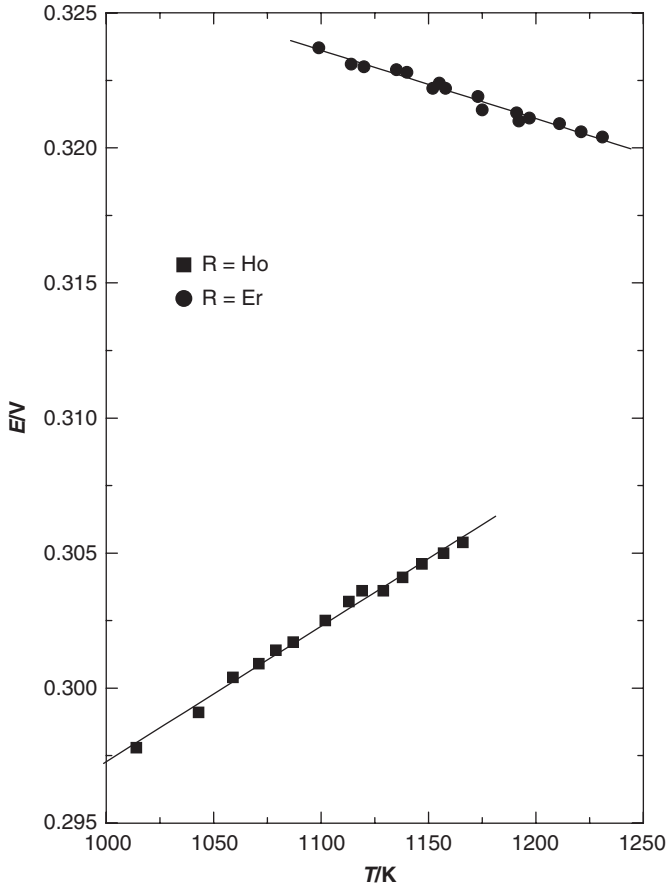

Fig. 7. Plot of e.m.f. against T for cell (I).

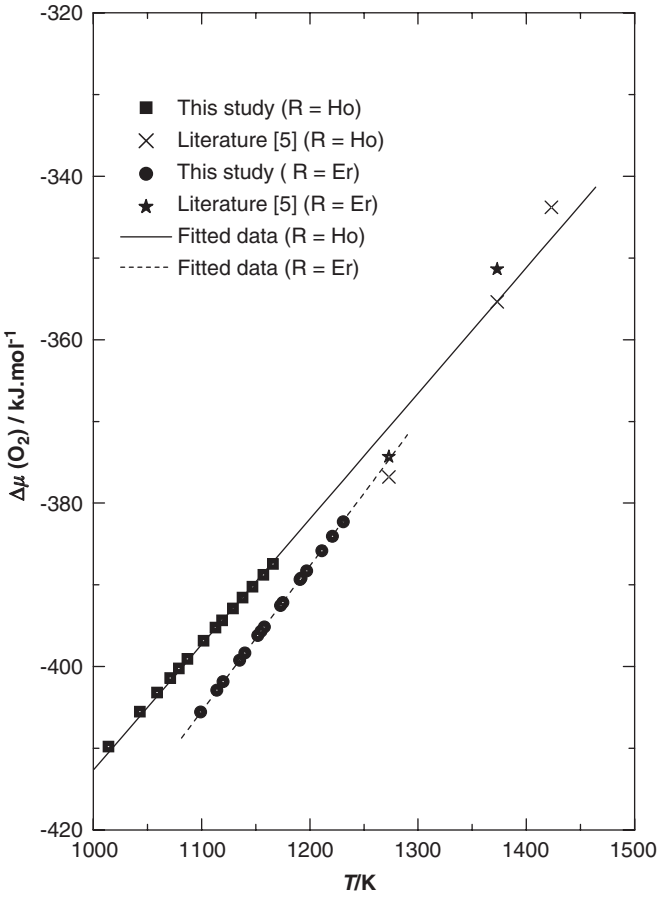

Fig. 8. Plot of $\Delta\mu(O_2)$ against T over the coexisting phases: $\{RFeO_3(s) + R_2O_3(s) + Fe(s)\}$ for $R = Ho$ and Er.

therefore to calculate the values of $\Delta\mu(O_2)$ in the whole temperature range by least-squares regression analysis of both sets of data. Thus the values calculated are given by

$$\{\Delta\mu(O_2)/kJ\,mol^{-1}\} \pm 1.9 = -566.6 + 0.1538\,(T/K) \quad (1014 \leqslant T/K \leqslant 1423)\ (\text{for } R = Ho), \tag{7}$$

$$\{\Delta\mu(O_2)/kJ\,mol^{-1}\} \pm 1.9 = -599.2 + 0.1762\,(T/K) \quad (1099 \leqslant T/K \leqslant 1273)\ (\text{for } R = Er). \tag{8}$$

The values of $\Delta_f G^o_m$ ($RFeO_3$, s) have been obtained using Eqs. (7) and (8) and $\Delta_f G^o_m$ (R_2O_3, s) from Barin [35]. The standard molar Gibbs energy of formation of $RFeO_3(s)$ from elements are given by

$$\{\Delta_f G^o_m(HoFeO_3,\ s)/kJ\,mol^{-1}\} \pm 3.2 = -1357.3 + 0.2524\,(T/K) (1014 \leqslant T/K \leqslant 1423), \tag{9}$$

$$\{\Delta_f G^o_m(ErFeO_3,\ s)/kJ\,mol^{-1}\} \pm 3.2 = -1391.5 + 0.2723\,(T/K) (1099 \leqslant T/K \leqslant 1273). \tag{10}$$

The temperature independent and temperature dependent terms in Eqs. (9) and (10) correspond to $\Delta_f H^o_m(T_{av})$ and $\Delta_f S^o_m(T_{av})$, respectively, with T_{av} being the average temperature. The standard Gibbs energies of formation of $RFeO_3(s)$ from the component oxides $R_2O_3(s)$ and $Fe_2O_3(s)$ according to the reaction:

$$\tfrac{1}{2}R_2O_3(s) + \tfrac{1}{2}Fe_2O_3(s) = RFeO_3(s), \tag{11}$$

are given by

$$\{\Delta_{ox} G^o_m/kJ\,mol^{-1}\} \pm 2.4 = -22.6 - 0.0070\ (T/K) (1014 \leqslant T/K \leqslant 1423)\ (\text{for } R = Ho), \tag{12}$$

$$\{\Delta_{ox} G^o_m/kJ\,mol^{-1}\} \pm 2.4 = -46.9 + 0.0097\ (T/K) (1099 \leqslant T/K \leqslant 1273)\ (\text{for } R = Er). \tag{13}$$

3.4. Oxygen chemical potential over the three-phase electrode $\{R_3Fe_5O_{12}\ (s) + RFeO_3(s) + Fe_3O_4(s)\}$

The reversible e.m.f.s of the following cell have been measured as a function of temperature.

Cell (II): $(-)Pt/\{R_3Fe_5O_{12}\ (s) + RFeO_3(s) + Fe_3O_4(s)\}$ //YDT/CSZ//$\{Ni(s) + NiO(s)\}$/Pt(+).

The variation of e.m.f. for cell (II) as a function of temperature are shown in Fig. 9. The e.m.f. data were

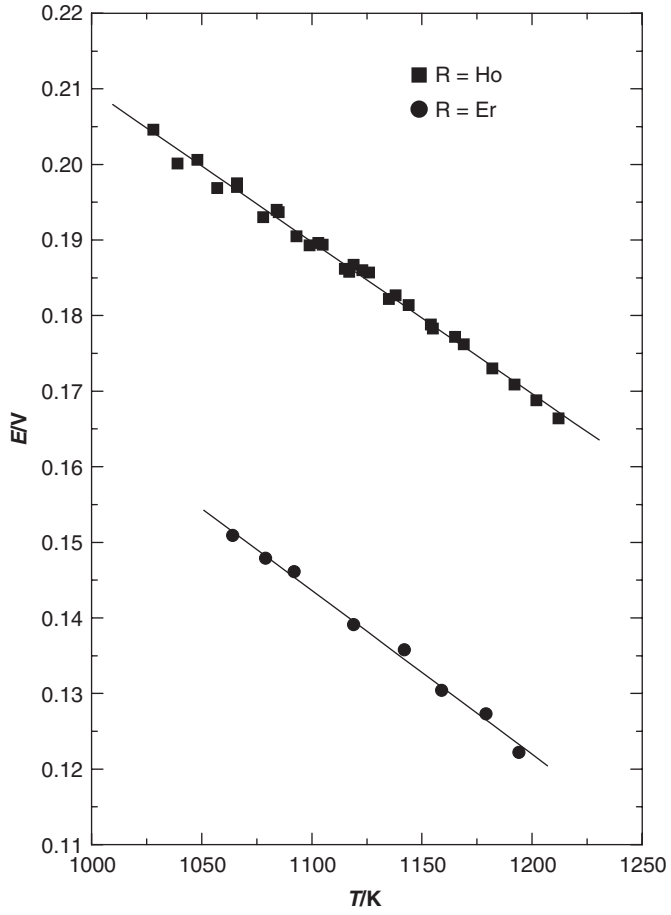

Fig. 9. Plot of e.m.f. against T for cell (II) with R = Ho and Er.

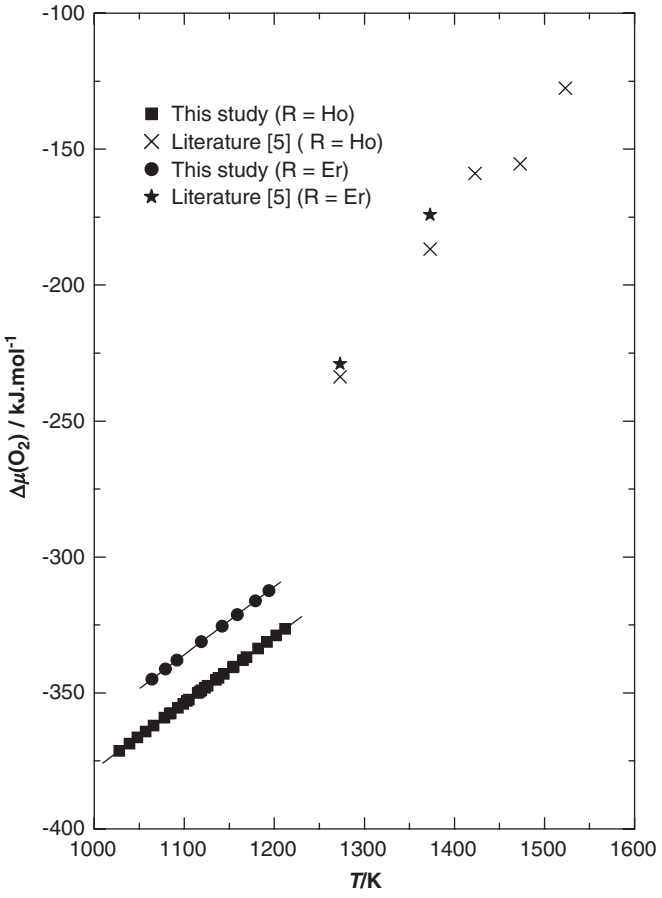

Fig. 10. Plot of $\Delta\mu(O_2)$ against T for the coexisting phase: $\{R_3Fe_5O_{12}(s) + RFeO_3(s) + Fe_3O_4(s)\}$.

least-squares fitted to give the relation:

$$E/\mathrm{V}\ (\pm 0.0008) = 0.4109 - 2.0099 \times 10^{-4}\ (T/\mathrm{K}) \quad (1028 \leqslant T/\mathrm{K} \leqslant 1212)\ (\text{for } R = \mathrm{Ho}), \tag{14}$$

$$E/\mathrm{V}\ (\pm 0.0008) = 0.3821 - 2.1675 \times 10^{-4}\ (T/\mathrm{K}) \quad (1064 \leqslant T/\mathrm{K} \leqslant 1194)\ (\text{for } R = \mathrm{Er}). \tag{15}$$

The oxygen chemical potential corresponding to three-phase mixture $\{R_3Fe_5O_{12}\ (s) + RFeO_3(s) + Fe_3O_4(s)\}$ in cell (II) has been calculated using the values of oxygen chemical potential for the phase mixture $\{Ni(s) + NiO(s)\}$ from the literature [35] and the values of e.m.f. obtained in the present study. For the equilibrium reaction:

$$18RFeO_3(s) + 4Fe_3O_4(s) + O_2(g) = 6R_3Fe_5O_{12}(s), \tag{16}$$

the results obtained can be represented by the following expressions:

$$\{\Delta\mu(O_2)/\mathrm{kJ\,mol^{-1}}\} \pm 0.5 = -622.1 + 0.2439\ (T/\mathrm{K}) \quad (1028 \leqslant T/\mathrm{K} \leqslant 1212)\ (\text{for } R = \mathrm{Ho}), \tag{17}$$

$$\{\Delta\mu(O_2)/\mathrm{kJ\,mol^{-1}}\} \pm 0.5 = -611.0 + 0.2501\ (T/\mathrm{K}) \quad (1064 \leqslant T/\mathrm{K} \leqslant 1194)\ (\text{for } R = \mathrm{Er}). \tag{18}$$

Kimizuka et al. [7] have reported the equilibrium oxygen chemical potential for reaction (16) at $T = 1273$, 1373, 1423, 1473 and 1523 K for R = Ho and at $T = 1273$ and 1373 K for R = Ho. The values of $\Delta\mu(O_2)$ obtained in the present study are compared with those reported by Kimizuka et al. [7] in Fig. 10. It is apparent that the results obtained in this study when extrapolated to higher temperatures are significantly lower than the values reported by Kimizuka et al. [7]. The slope of the oxygen chemical potential deduced from the values of Kimizuka et al. [7] gives an unacceptably low value for the partial molar entropy of oxygen in equilibrium with the three condensed phases. It was decided therefore to select the results obtained in the present study alone to calculate other thermodynamic functions. The values of $\Delta_f G^o_m$ ($R_3Fe_5O_{12}$, s) have been obtained using Eqs. (17) and (18), $\Delta_f G^o_m$ ($RFeO_3$, s) from Eqs. (9) and (10) and $\Delta_f G^o_m$ (Fe_3O_4, s) from the literature [35].

The standard molar Gibbs energies of formation of $R_3Fe_5O_{12}(s)$ from elements are given by

$$\{\Delta_f G^o_m(Ho_3Fe_5O_{12},\ s)/\mathrm{kJ\,mol^{-1}}\} \pm 2.6 = -4899.9 + 0.9970\,(T/\mathrm{K})\ (1028 \leqslant T/\mathrm{K} \leqslant 1212), \tag{19}$$

$$\{\Delta_f G^o_m(Er_3Fe_5O_{12},\ s)/kJ\,mol^{-1}\} \pm 2.6 = -5000.6 + 1.0579\,(T/K)\ (1064 \leqslant T/K \leqslant 1194). \quad (20)$$

Standard molar enthalpy $\Delta_f H^o_m(T_{av})$ and entropy of formation $\Delta_f S^o_m(T_{av})$ at an average temperature (T_{av}) can be obtained from the temperature independent and temperature dependent terms in Eqs. (19) and (20). The standard molar Gibbs energy of formation of $R_3Fe_5O_{12}$(s) from its component oxides R_2O_3(s) and Fe_2O_3(s) according to the reaction:

$$\tfrac{3}{2}R_2O_3(s) + \tfrac{5}{2}Fe_2O_3(s) = R_3Fe_5O_{12}(s), \quad (21)$$

are given by

$$\{\Delta_{ox} G^o_m/kJ\,mol^{-1}\} \pm 3.5 = -90.9 - 0.0261\ (T/K)(1028 \leqslant T/K \leqslant 1212)\ (\text{for } R = Ho), \quad (22)$$

$$\{\Delta_{ox} G^o_m/kJ\,mol^{-1}\} \pm 3.5 = -162.4 - 0.0252\ (T/K)(1064 \leqslant T/K \leqslant 1194)\ (\text{for } R = Er). \quad (23)$$

3.5. Oxygen chemical potential over the three-phase electrode {RFe_2O_4(s)+R_2O_3(s)+Fe(s)}

The reversible e.m.f.s of the following cell have been measured as a function of temperature.

$$\text{Cell (III)}: (-)Pt/\{RFe_2O_4(s) + R_2O_3(s) + Fe(s)\}\ //CSZ//\{air,\ p(O_2) = 21.12\,kPa\}/Pt(+).$$

For R = Ho, e.m.f. measurements were carried out in two different temperature ranges: 1389–1523 K (set I) and 1322–1535 K (set II) using the high temperature cell assembly. The values of e.m.f. for cell (III) as a function of temperature are shown in Fig. 11. It has been observed from both sets of data that the e.m.f. below 1443 K was not stable. This could be due to change in the coexisting three-phase field. Hence, data above 1443 K are considered for further calculations for R = Ho. Similarly, for R = Er, two different sets of measurements in the temperature ranges: 1373–1535 K (set I) and 1370–1520 K (set II) were carried out. The variation of e.m.f. with temperature is shown in Fig. 12. It has been observed that the e.m.f. data obtained in the two sets of measurements are in good agreement with each other which indicates that the three coexisting phases are in equilibrium in these temperature ranges. The e.m.f. data were least-squares fitted to give the relations;

$$E/V\ (\pm 0.0013) = 1.2517 - 2.7820 \times 10^{-4}(T/K)\ (1443 \leqslant T/K \leqslant 1535)\ (\text{for } R = Ho), \quad (24)$$

$$E/V\ (\pm 0.0013) = 1.2794 - 2.9640 \times 10^{-4}(T/K)\ (1370 \leqslant T/K \leqslant 1535)\ (\text{for } R = Er). \quad (25)$$

The oxygen chemical potential corresponding to three-phase mixtures {RFe_2O_4(s) + R_2O_3(s) + Fe(s)} in cell (III) have been calculated using Eqs. (24) and (25) and the values of oxygen partial pressure of air ($p(O_2)$ = 21.12 kPa). For the equilibrium reaction:

$$\tfrac{2}{5}R_2O_3(s) + \tfrac{8}{5}Fe(s) + O_2(g) = \tfrac{4}{5}RFe_2O_4(s), \quad (26)$$

the results obtained can be represented by the following expressions:

$$\{\Delta\mu(O_2)/kJ\,mol^{-1}\} \pm 0.8 = -483.1 + 0.0941\ (T/K)\ (1443 \leqslant T/K \leqslant 1535)\ (\text{for } R = Ho), \quad (27)$$

$$\{\Delta\mu(O_2)/kJ\,mol^{-1}\} \pm 0.8 = -493.8 + 0.1014\ (T/K)\ (1370 \leqslant T/K \leqslant 1535)\ (\text{for } R = Er). \quad (28)$$

The oxygen chemical potential for the three-phase mixture {RFe_2O_4(s) + R_2O_3(s) + Fe(s)} have been reported by Kimizuka et al. [7] at two different temperatures: (1473 and 1523 K) for R = Ho and (1373 and 1473 K) for R = Er. The values obtained in this study are compared with those of Kimizuka et al. [7] in Figs. 13 and 14.

It has been observed that the oxygen potential obtained in the present study is more negative by ~6 kJ mol^{-1} than the values reported by Kimizuka et al. [7] for R = Ho and by ~8 kJ mol^{-1}. The values of $\Delta_f G^o_m$ (RFe_2O_4, s) have been obtained using Eqs. (27) and (28) and $\Delta_f G^o_m$ (R_2O_3, s) from Barin [35]. The standard molar Gibbs energies of formation of RFe_2O_4(s) from elements are given by

$$\{\Delta_f G^o_m(HoFe_2O_4,\ s)/kJ\,mol^{-1}\} \pm 3.2 = -1536.3 + 0.2550\,(T/K)\ (1443 \leqslant T/K \leqslant 1535), \quad (29)$$

$$\{\Delta_f G^o_m(ErFe_2O_4,\ s)/kJ\,mol^{-1}\} \pm 3.2 = -1559.4 + 0.2670\,(T/K)\ (1370 \leqslant T/K \leqslant 1535). \quad (30)$$

The temperature independent and temperature dependent terms in Eqs. (29) and (30) correspond to $\Delta_f H^o_m(T_{av})$ and $\Delta_f S^o_m(T_{av})$, respectively, with T_{av} being the average temperature.

3.6. Isothermal oxygen potential diagram

In oxide systems, the oxygen partial pressure is often established by the ratio of CO to CO_2 or H_2 to H_2O in the gas phase. Therefore, it is useful to represent phase relations as a function of partial pressure of oxygen and such a diagram is called oxygen potential diagram. The oxygen potential diagram is a plot of oxygen potential as a function of a normalized composition parameter. The composition variable is the cationic fraction, $\eta_A/(\eta_A + \eta_B)$, where η_A and η_B represent moles of components 'A' and 'B' in the system A–B–O. Oxygen is not included in the composition parameter. Intermetallic phases and binary oxides are represented by vertical lines. Nonstoichiometry in intermetallics and cation nonstoichiometry in ternary oxides can be displayed on the diagram. However, oxygen nonstoichiometry cannot be displayed since oxygen is not included in the normalized composition parameter. The diagram provides useful information on the oxygen potential range for the stability of the various phases. All

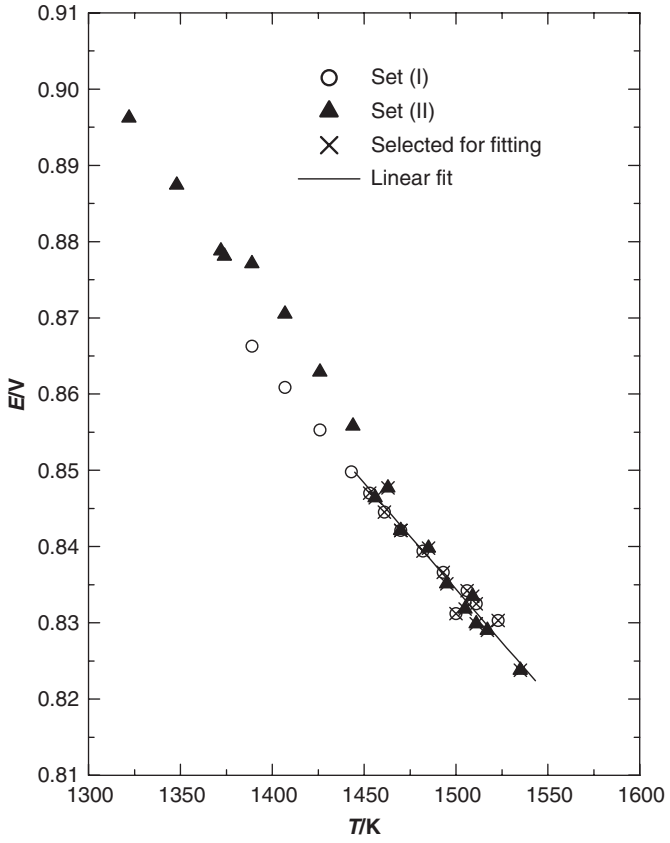

Fig. 11. Plot of e.m.f. against T for cell (III) with $R = \mathrm{Ho}$.

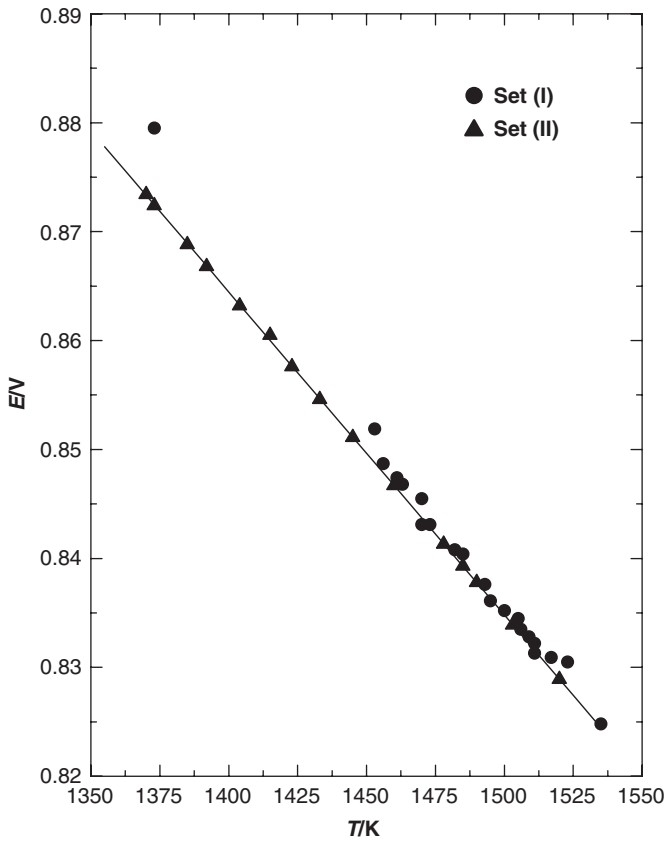

Fig. 12. Plot of e.m.f. against T for cell (III) with $R = \mathrm{Er}$.

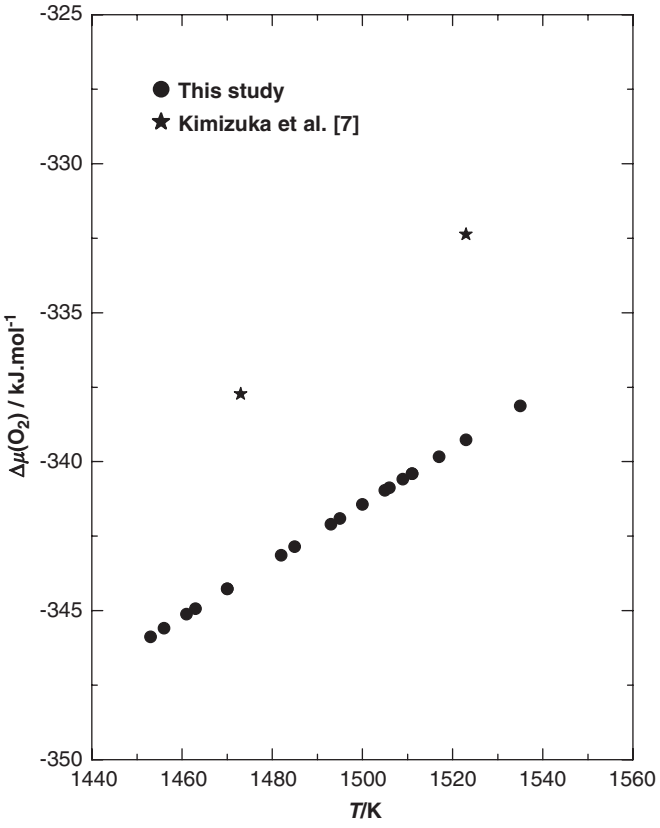

Fig. 13. Plot of oxygen potential against T for the three-phase mixture: $\{HoFe_2O_4(s) + Ho_2O_3(s) + Fe(s)\}$.

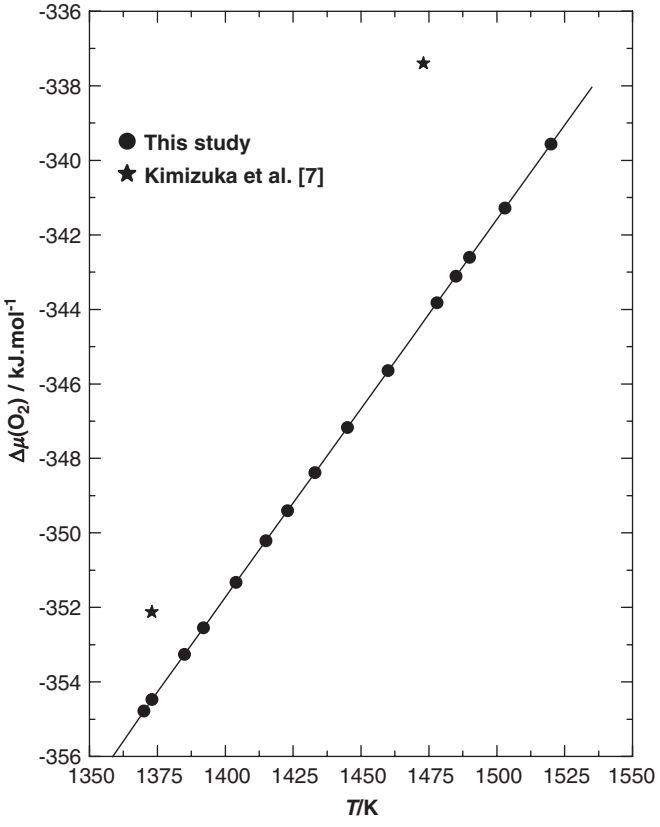

Fig. 14. Plot of oxygen potential against T for the three-phase mixture: $\{ErFe_2O_4(s) + Er_2O_3(s) + Fe(s)\}$.

the topological rules of construction for conventional temperature-composition phase diagrams are applicable to the isothermal oxygen potential diagram. When three condensed phases coexist at equilibrium with a gas phase in a ternary system such as A–B–O, the system is univariant; at a fixed temperature three condensed phases coexist only at a unique partial pressure of oxygen. Therefore, horizontal lines on the diagram represent three-phase equilibrium. The diagram is complementary to the conventional Gibbs triangle representation of phase relations in ternary systems, where the composition of each phase can be unambiguously displayed.

The oxygen potential diagram for the systems R–Fe–O at $T = 1250$ and 1450 K, computed from the results of this study and the data for the binary systems R–O and Fe–O from Barin [35] and Sundman [36], respectively, are shown in Figs. 15 and 16 for $R =$ Ho and in Figs. 17 and 18 for $R =$ Er. The oxygen chemical potentials corresponding to alloy-oxide equilibria are not shown in these figures because their thermodynamic data are not available in the literature. The diagrams contructed at two different temperatures are different because at low temperature (1250 K) $R\mathrm{Fe_2O_4}$(s) is unstable whereas at high temperature (1450 K) this phase is stable. Accordingly, the three-phase equilibria are different at these two temperatures. Similar oxygen potential diagrams at other temperatures could be readily computed from the thermodynamic data if required for a specific application. The two- and three-dimensional chemical potential diagrams for this system are not computed because the thermodynamic data for alloys/intermetallics are not available in the literature.

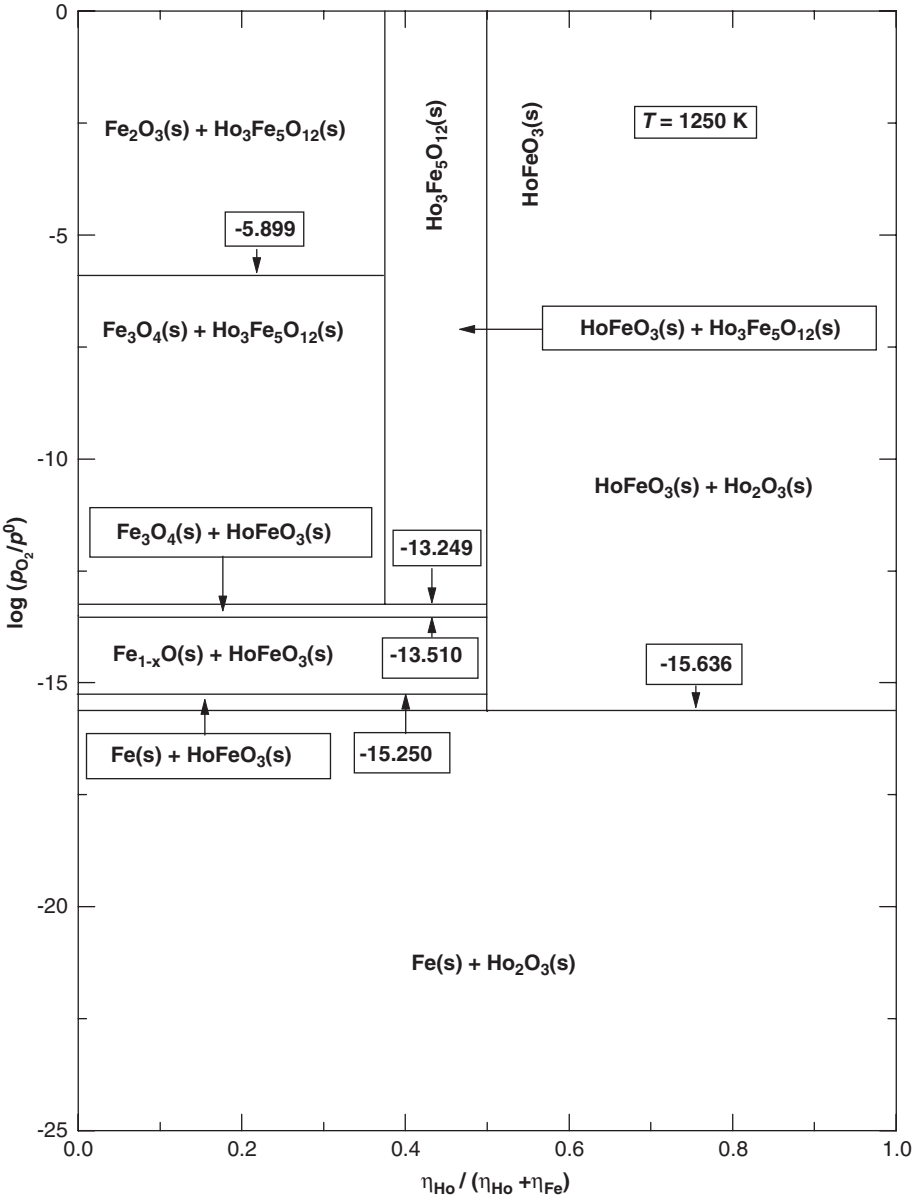

Fig. 15. Isothermal oxygen potential diagram for the system Ho–Fe–O at 1250 K.

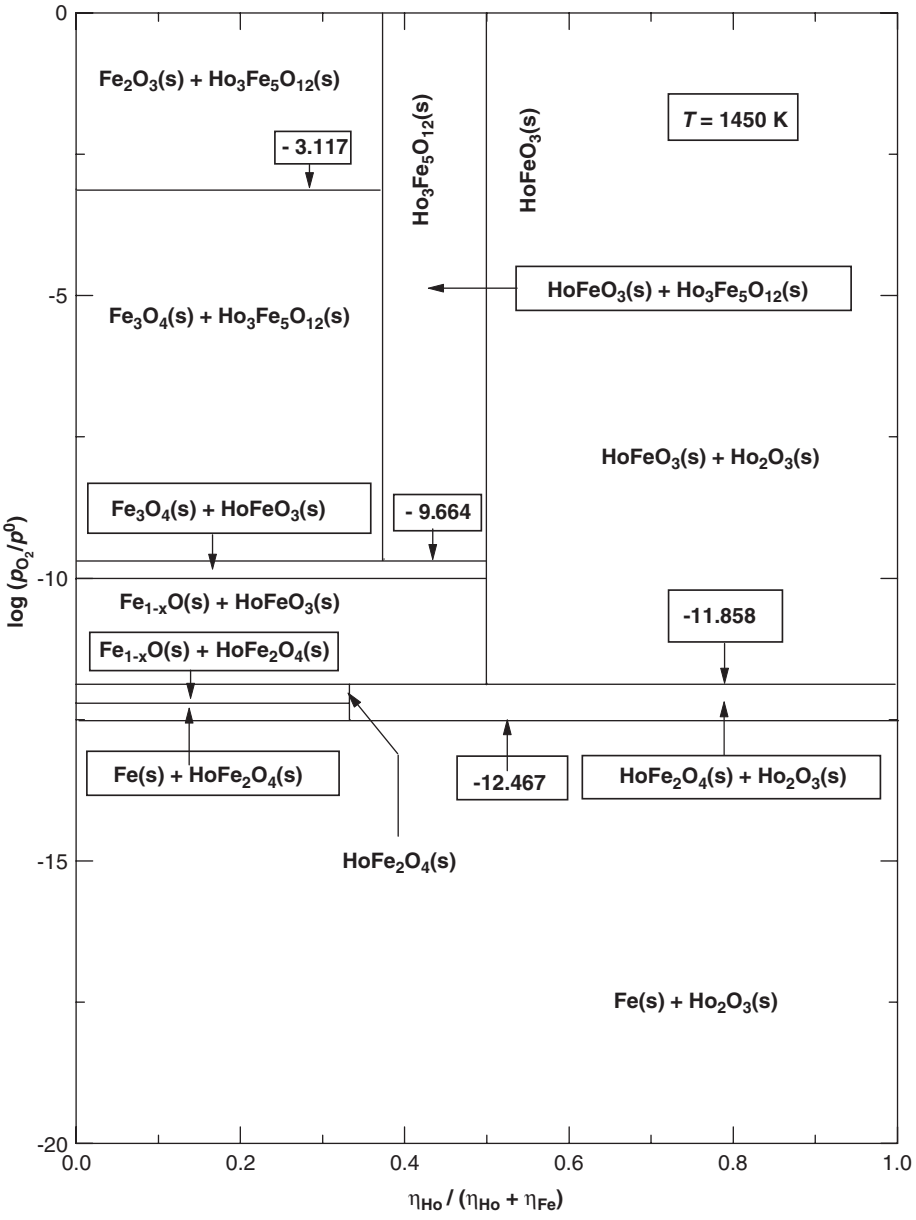

Fig. 16. Isothermal oxygen potential diagram for the system Ho–Fe–O at 1450 K.

3.7. Construction of thermodynamic table

The entropy increment $\{S^{o}_{m}(T) - S^{o}_{m}(0)\}$ and the enthalpy increment $\{H^{o}_{m}(T) - H^{o}_{m}(0)\}$ functions are calculated by numerical integration of the $C^{o}_{p}(T)/T$ and $C^{o}_{p}(T)$ functions, respectively. These functions are constructed using polynomial fit of the $C^{o}_{p}(T)$ curve in small temperature ranges. The Gibbs energy, $\{G^{o}_{m}(T) - H^{o}_{m}(0)\}$ is calculated by using the relation:

$$\{G^{o}_{m}(T) - H^{o}_{m}(0)\} = \{H^{o}_{m}(T) - H^{o}_{m}(0)\} - TS^{o}_{m}(T). \quad (31)$$

The values of $\{H^{o}_{m}(T) - H^{o}_{m}(298.15\,K)\}$ are calculated by using the relation:

$$\{H^{o}_{m}(T) - H^{o}_{m}(298.15\,K)\} = \{H^{o}_{m}(T) - H^{o}_{m}(0)\} - \{H^{o}_{m}(298.15\,K) - H^{o}_{m}(0)\}. \quad (32)$$

In order to make full use of the thermodynamic data, $G^{o}_{m}(T)$ should be evaluated which requires a known value of $H^{o}_{m}(0)$. However, absolute value of $H^{o}_{m}(0)$ is difficult to determine or calculate. Therefore, first $H^{o}_{m}(T)$ is calculated using the relation:

$$H^{o}_{m}(T) = \Delta_{f}H^{o}_{298.15\,K} + \int_{298.15}^{T} C^{o}_{p,m}(T)\,dT. \quad (33)$$

The absolute value of $S^{o}_{m}(T)$ is calculated using the $S^{o}_{m}(0) = 0$ and the relation:

$$S^{o}_{m}(T) = \int_{0}^{T} \frac{C^{o}_{p,m}(T)}{T}\,dT. \quad (34)$$

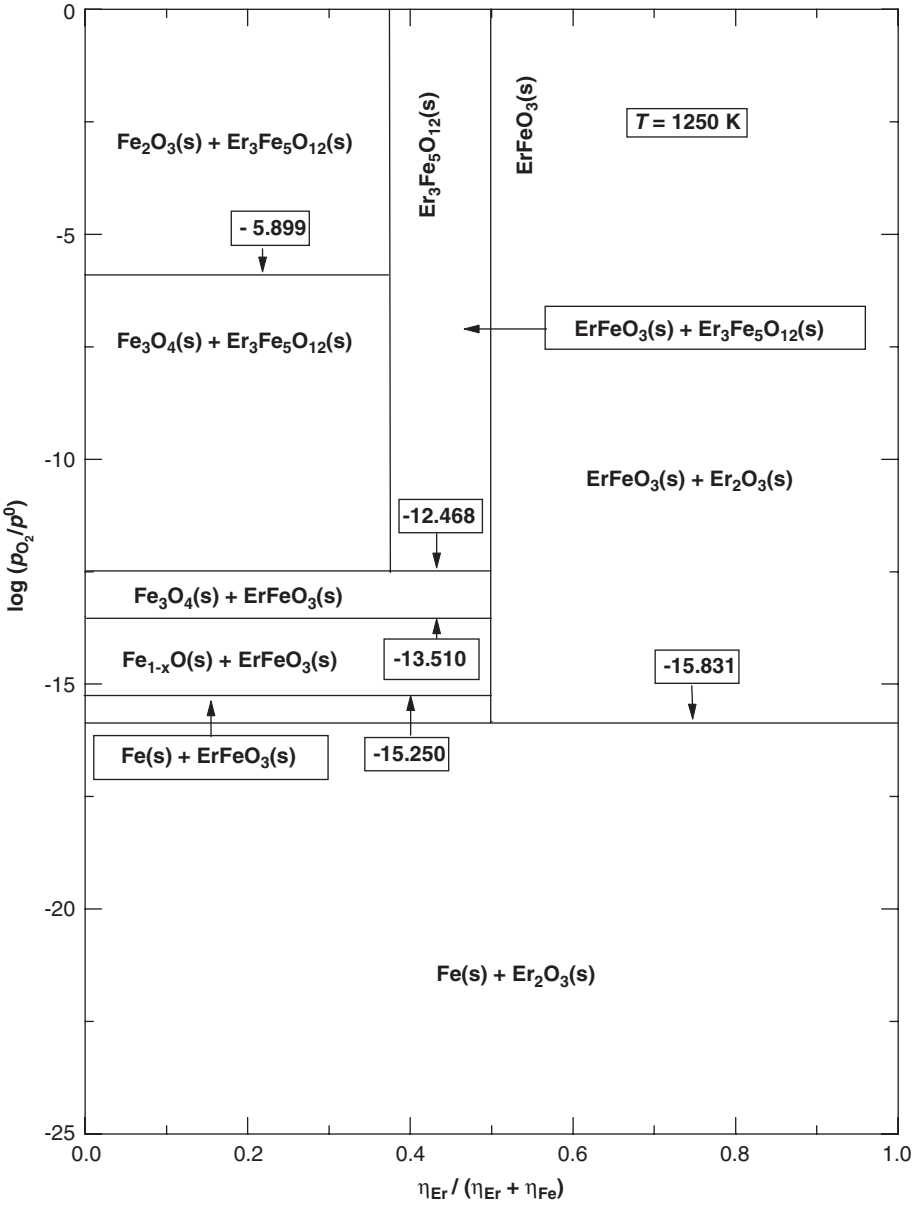

Fig. 17. Isothermal oxygen potential diagram for the system Er–Fe–O at 1250 K.

Now $G^{o}_{m}(T)$ can be calculated using the relation:

$$G^{o}_{m}(T) = H^{o}_{m}(T) - TS^{o}_{m}(T). \quad (35)$$

The free energy function (or the Plank's function) $\Phi^{o}_{m}(T)$ is calculated using the relation:

$$\Phi^{o}_{m}(T) = -\left\{\frac{G^{o}_{m}(T) - H^{o}_{m}(298.15\,K)}{T}\right\}. \quad (36)$$

After calculation of all the thermodynamic functions, the values are tabulated at selected temperatures. The thermodynamic functions which are usually tabulated in tables are: $C^{o}_{p,m}$, S^{o}_{m}, $\{H^{o}_{m}(T) - H^{o}_{m}(298.15\,K)\}$, H^{o}_{m}, $\Phi^{o}_{m}(T)$, $\Delta_f H^{o}_{m}(T)$ and $\Delta_f G^{o}_{m}(T)$. The values generated in this study for RFeO$_3$(s) and R_3Fe$_5$O$_{12}$(s) are listed in Tables 3–6.

4. Discussion

Earlier studies by the present authors [13–18] on the thermodynamic properties of ternary oxides in the systems R–Fe–O include enthalpy increment measurements for RFeO$_3$(s) (R = La, Nd, Sm, Dy), R_3Fe$_5$O$_{12}$(s) (R = Sm, Dy) and Gibbs energy of formation of RFeO$_3$(s) (R = La, Nd, Sm, Eu, Gd, Tb, Dy) and R_3Fe$_5$O$_{12}$(s) (R = Sm, Eu, Gd, Tb, Dy). The present study completes the series up to R = Er. However, it is imperative to mention here that thermodynamic data for other ternary oxides in the series for R = Tm, Yb and Lu are required to obtain a systematic description of structure-property relations in these types of oxides. Since the complexity of phase relations increase for

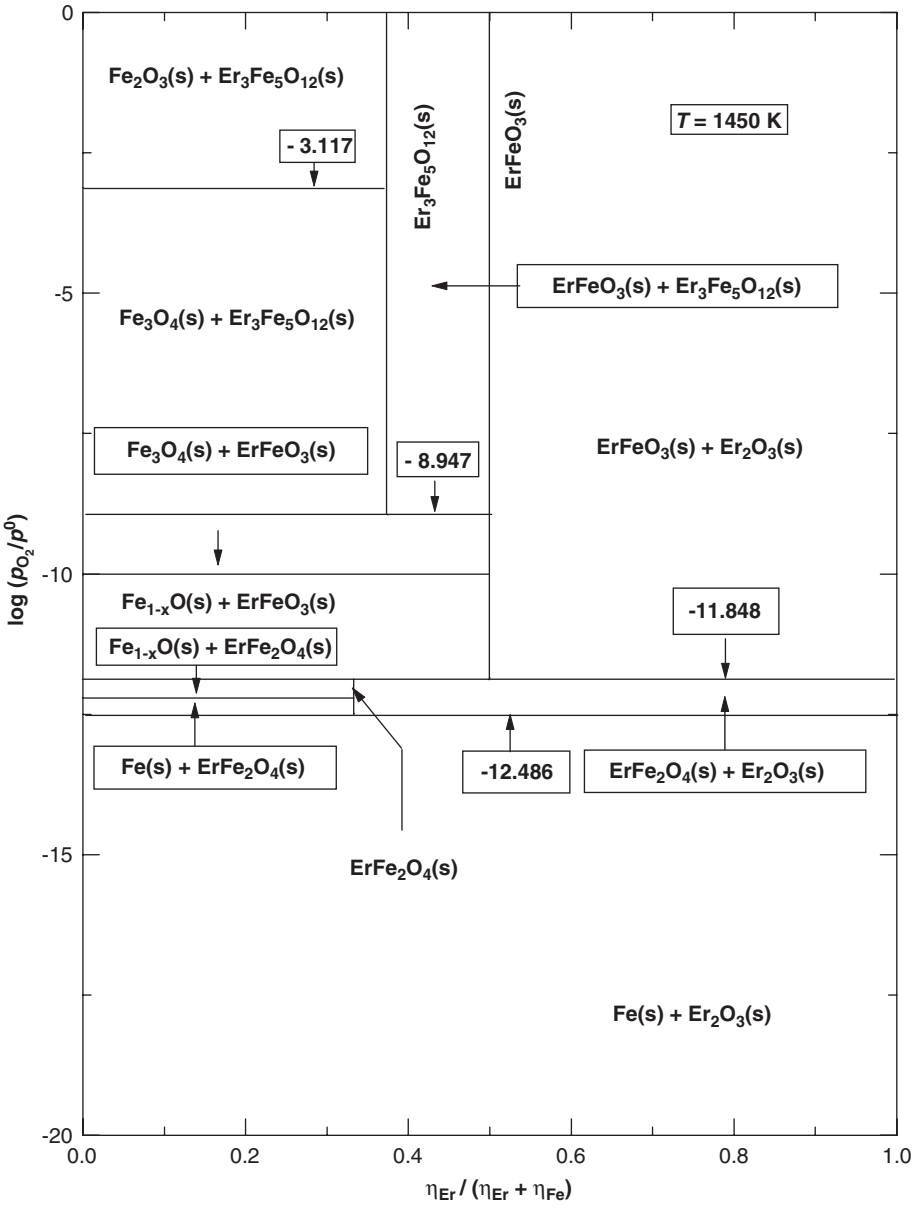

Fig. 18. Isothermal oxygen potential diagram for the system Er–Fe–O at 1450 K.

R = Tm to Lu with appearance of new phases, more number of experiments need to be carried out to determine the thermodynamic properties of the complete system. The present authors are making an attempt to find a semi-empirical model approach to predict the thermodynamic properties of these oxides without tedious experiments.

A comprehensive thermodynamic data for all these compounds coupled to the available phase diagram information can be used to derive a consistent set of thermodynamic parameters by the CALPHAD (acronym for CALculation of PHAse Diagrams) approach which can pave the way to calculate multicomponent phase diagrams involving these basic elements.

5. Conclusions

Ternary oxides in the systems R–Fe–O (R = Ho and Er) have been prepared and characterized using X-ray diffraction analysis. Solid-state electrochemical cells employing oxide electrolytes have been used to measure the oxygen chemical potential over the coexisting phase mixtures $\{RFeO_3(s) + R_2O_3(s) + Fe(s)\}$ and $\{R_3Fe_5O_{12}(s) + RFeO_3(s) + Fe_3O_4(s)\}$ and $\{RFe_2O_4(s) + R_2O_3(s) + Fe(s)\}$. The standard molar Gibbs energies of formation of $RFeO_3(s)$, $R_3Fe_5O_{12}(s)$ and $RFe_2O_4(s)$ have been calculated from the oxygen potential data and presented in analytic forms. Isothermal oxygen potential diagrams have been computed for the systems R–Fe–O at 1250 and 1450 K.

Table 3
Thermodynamic data for $HoFeO_3$(s)

T/K	S°_T / J K^{-1} mol^{-1}	$C^\circ_{p,m}$/ J K^{-1} mol^{-1}	$H^\circ_T - H^\circ_0$/ J mol^{-1}	$H^\circ_T - H^\circ_{298.15}$/J mol^{-1}	H°_T/ J mol^{-1}	G°_T/J mol^{-1}	$-(G^\circ_T - H^\circ_{298.15})/T$/ J K^{-1} mol^{-1}	$\Delta_f H^\circ_m$/ kJ mol^{-1}	$\Delta_f G^\circ_m$/ kJ mol^{-1}
0	0	0	0						
25	6.789	6.520	69.4050						
50	16.20	22.77	432.690						
75	28.08	36.51	1176.45						
100	40.27	48.44	2242.51						
150	63.96	70.04	5200.44						
200	86.68	87.59	9169.31						
250	107.6	99.22	13861.2						
298.15	125.7	109.0	18822.1	0	−1364200	−1401677	125.7	−1364.2	−1279.5
300	126.3	109.3	19024.5	202.4	−1363998	−1401910	125.7	−1364.1	−1278.9
325	135.3	112.6	21808.2	2986.1	−1361223	−1405182	126.1	−1363.8	−1271.8
350	143.7	115.6	24676.0	5853.9	−1358369	−1408670	126.9	−1363.4	−1264.8
400	159.5	121.1	30628.6	11806.5	−1352449	−1416256	130.0	−1362.4	−1250.8
450	174.1	126.5	36845.9	18023.8	−1346262	−1424601	134.0	−1361.3	−1236.9
500	187.7	132.5	43344.7	24522.6	−1339792	−1433649	138.7	−1359.9	−1223.1
550	200.7	140.1	50195.4	31373.3	−1332987	−1443362	143.6	−1358.4	−1209.5
600	213.3	150.8	57521.8	38699.7	−1325734	−1453712	148.8	−1356.5	−1196.1
644	224.4	165.7	64502.1	45680.0	−1318796	−1463341	153.5	−1354.4	−1184.4
644	224.4	165.7	64502.1	45680.0	−1318796	−1463341	153.5	−1354.4	−1184.4
650	225.7	137.3	65315.1	46493.0	−1317968	−1464692	154.2	−1354.2	−1182.7
700	235.6	130.3	71977.7	53155.6	−1311309	−1476230	159.7	−1353.2	−1169.6
750	244.5	127.5	78468.3	59646.2	−1304871	−1488236	164.9	−1352.5	−1156.6
800	252.7	126.1	84827.8	66005.7	−1298534	−1500667	170.2	−1352.0	−1143.5
850	260.3	125.3	91097.2	72275.1	−1292250	−1513493	175.3	−1351.8	−1130.5
900	267.4	124.9	97317.5	78495.4	−1285996	−1526688	180.2	−1351.7	−1117.5
950	274.2	124.7	103529	84707.6	−1279758	−1540230	185.0	−1351.9	−1104.4
1000	280.6	124.5	109775	90952.6	−1273528	−1554100	189.6	−1352.5	−1091.4

Table 4
Thermodynamic data for $ErFeO_3$(s)

T/K	S°_T/ J K^{-1} mol^{-1}	$C^\circ_{p,m}$/ J K^{-1} mol^{-1}	$H^\circ_T - H^\circ_0$/ J mol^{-1}	$H^\circ_T - H^\circ_{298.15}$/ J mol^{-1}	H°_T/J mol^{-1}	G°_T/J mol^{-1}	$-(G^\circ_T - H^\circ_{298.15})/T$/ J K^{-1} mol^{-1}	$\Delta_f H^\circ_m$/ kJ mol^{-1}	$\Delta_f G^\circ_m$/ kJ mol^{-1}
0	0	0	0						
25	9.262	7.757	85.7410						
50	18.78	21.21	448.534						
75	29.85	34.19	1142.01						
100	41.42	46.73	2154.60						
150	64.91	70.37	5091.89						
200	87.73	87.95	9079.50						
250	108.7	100.0	13795.1						
298.15	127.2	109.8	18839.5	0	−1400500	−1438424	127.2	−1400.5	−1316.8
300	127.9	110.1	19042.4	202.9	−1400296	−1438660	127.2	−1400.4	−1316.2
325	136.8	113.6	21837.6	2998.1	−1397499	−1441970	127.6	−1400.1	−1309.2
350	145.4	116.8	24720.7	5881.2	−1397618	−1445499	128.6	−1399.7	−1302.3
400	161.4	122.8	30715.7	11876.2	−1388626	−1453173	131.7	−1398.7	−1288.4
450	176.2	128.9	36993.4	18153.9	−1382334	−1461616	135.8	−1397.5	−1274.7
500	190.1	135.8	43578.9	24739.4	−1375722	−1470776	140.6	−1396.0	−1261.1
550	203.4	144.5	50557.1	31717.6	−1368726	−1480616	145.8	−1394.3	−1247.7
600	216.5	156.9	58072.2	39232.7	−1361212	−1491115	151.1	−1392.2	−1234.4
634	225.5	169.6	63590.6	44751.1	−1355673	−1498629	154.9	−1390.4	−1225.6
634	225.5	169.6	63590.6	44751.1	−1355673	−1498629	154.9	−1390.4	−1225.6
650	228.9	139.3	65821.4	46981.9	−1353419	−1502265	156.7	−1389.9	−1221.4
700	239.1	134.3	72638.2	53798.7	−1346602	−1513971	162.2	−1388.8	−1208.5
750	248.3	132.6	79298.8	60459.3	−1339936	−1526159	167.7	−1387.9	−1195.7
800	256.8	132.0	85884.3	67044.8	−1333325	−1538790	173.0	−1387.2	−1182.9
850	264.8	132.0	92452.4	73612.9	−1326726	−1551834	178.6	−1386.7	−1170.1
900	272.4	132.3	99037.4	80197.9	−1320119	−1565266	183.3	−1386.4	−1157.4
950	279.6	132.8	105650	86810.9	−1313493	−1579066	188.2	−1386.3	−1144.7
1000	286.4	133.4	112279	93439.4	−1306839	−1593216	192.9	−1386.4	−1131.9

Table 5
Thermodynamic data for $Ho_3Fe_5O_{12}$(s)

T/K	S°_T/ J K^{-1} mol^{-1}	$C^\circ_{p,m}$/ J K^{-1} mol^{-1}	$H^\circ_T - H^\circ_0$/ J mol^{-1}	$H^\circ_T - H^\circ_{298.15}$/ J mol^{-1}	H°_T/J mol^{-1}	G°_T/J mol^{-1}	$-(G^\circ_T - H^\circ_{298.15})/T$/ J K^{-1} mol^{-1}	$\Delta_f H^\circ_m$/ kJ mol^{-1}	$\Delta_f G^\circ_m$/ kJ mol^{-1}
0	0	0	0						
25	47.42	34.85	336.205						
50	84.57	76.81	1736.26						
75	123.4	117.7	4169.64						
100	162.8	156.4	7613.76						
150	242.6	241.5	17601.7						
200	322.7	317.1	31608.2						
250	400.8	383.3	49160.4						
298.15	473.1	445.7	68973.7	0	−4925600	−5066654	473.1	−4925.6	−4592.1
300	475.8	447.4	69799.6	825.9	−4924773	−5067532	473.1	−4925.4	−4590.0
325	512.4	467.4	81236.1	12262.3	−4913328	−5079889	474.7	−4923.6	−4562.1
350	547.7	483.9	93126.3	24152.5	−4901429	−5093146	478.7	−4921.4	−4534.4
400	614.1	510.0	117993.7	49020.0	−4876550	−5122216	491.6	−4916.3	−4479.4
450	675.4	531.4	144018.4	75044.7	−4850503	−5154477	508.7	−4910.5	−4425.1
500	732.5	552.6	171080.7	102107.0	−4823410	−5189695	528.3	−4904.0	−4371.6
546	782.2	577.3	197013.7	128040.0	−4797454	−5224543	547.7	−4897.5	−4322.9
546	782.2	577.3	197013.7	128040.0	−4797454	−5224543	547.7	−4897.5	−4322.9
550	786.2	548.2	199201.4	130227.6	−4795259	−5227680	549.4	−4897.0	−4318.6
600	833.7	545.1	226519.7	157545.9	−4767961	−5268197	571.1	−4891.3	−4266.3
650	877.3	546.0	253826.6	184852.8	−4740687	−5310989	592.9	−4886.2	−4214.4
700	917.9	547.7	281167.6	212193.9	−4713343	−5355884	614.7	−4881.5	−4163.0
750	955.7	549.4	308575.0	239601.2	−4685912	−5402736	636.3	−4877.3	−4111.8
800	991.2	551.0	336067.4	267093.6	−4658400	−5451421	657.4	−4873.7	−4060.9
850	1024.7	552.3	363650.1	294676.4	−4630814	−5501830	678.0	−4870.8	−4010.2
900	1056.3	553.5	391315.1	322341.4	−4603164	−5553863	698.1	−4868.8	−3959.6
950	1086.2	554.6	419040.9	350067.2	−4575457	−5607435	717.8	−4867.7	−3909.1
1000	1114.7	555.5	446792.7	377818.9	−4547702	−5662468	736.9	−4868.0	−3858.7

Table 6
Thermodynamic data for $Er_3Fe_5O_{12}$(s)

T/K	S°_T/ J K^{-1} mol^{-1}	$C^\circ_{p,m}$/ J K^{-1} mol^{-1}	$H^\circ_T - H^\circ_0$/ J mol^{-1}	$H^\circ_T - H^\circ_{298.15}$/ J mol^{-1}	H°_T/J mol^{-1}	G°_T/J mol^{-1}	$-(G^\circ_T - H^\circ_{298.15})/T$/ J K^{-1} mol^{-1}	$\Delta_f H^\circ_m$/ kJ mol^{-1}	$\Delta_f G^\circ_m$/ kJ mol^{-1}
0	0	0	0						
25	36.90	35.01	434.878						
50	70.81	69.04	1708.18						
75	105.6	105.2	3886.62						
100	141.0	142.8	6982.72						
150	214.9	232.0	16245.7						
200	292.7	309.7	29865.1						
250	368.9	373.3	46988.3						
298.15	483.9	428.0	66294.6	0	−5023500	−5167774	483.9	−5023.5	−4694.8
300	486.6	432.1	67092.3	797.6	−5022702	−5168672	483.9	−5023.4	−4692.8
325	521.9	452.2	78147.7	11853.0	−5011640	−5181281	485.5	−5022.0	−4665.3
350	556.1	468.8	89660.2	23365.6	−5000122	−5194760	489.3	−5020.2	−4637.9
400	620.5	495.3	113786.3	47491.6	−4975992	−5224197	501.7	−5016.0	−4583.6
450	680.1	517.3	139095.8	72801.2	−4950668	−5256732	518.3	−5010.9	−4529.8
500	735.8	539.2	165479.0	99184.3	−4924266	−5292144	537.3	−5005.3	−4476.6
544	782.2	563.6	189701.4	123406.7	−4900034	−5325546	555.3	−4999.7	−4430.4
544	782.2	563.6	189701.4	123406.7	−4900034	−5325546	555.3	−4999.7	−4430.4
550	788.0	534.2	192899.2	126604.6	−4896825	−5330256	557.8	−4999.1	−4424.1
600	834.4	532.1	219543.1	153248.4	−4870200	−5370835	578.9	−4994.2	−4372.0
650	877.0	533.7	246214.9	179920.3	−4843559	−5413634	600.2	−4989.8	−4320.4
700	916.7	536.1	272957.2	206662.6	−4816813	−5458489	621.4	−4985.9	−4269.0
750	953.7	538.4	299799.6	233504.9	−4789949	−5505260	642.4	−4982.4	−4218.0
800	988.6	540.7	326759.2	260464.6	−4762970	−5553826	662.9	−4979.6	−4167.1
850	1021.4	542.7	353840.7	287546.1	−4735885	−5604084	683.1	−4977.4	−4116.4
900	1052.5	544.6	381036.0	314741.4	−4708704	−5655938	702.8	−4975.9	−4065.8
950	1081.9	546.3	408324.6	342029.9	−4681433	−5709306	721.9	−4975.4	−4015.2
1000	1110.0	547.8	435673.1	369378.5	−4654081	−5764111	740.6	−4976.2	−3964.7

Thermodynamic functions have been generated for $RFeO_3$(s) and $R_3Fe_5O_{12}$(s).

References

[1] G. Heane, M. Pasternak, R. Taylor, Nuovo-Cimento. D 18D (1996) 145–161.
[2] A.E. Bocquet, A. Fujimori, T. Mizokawa, T. Saitoh, H. Namatame, S. Suga, N. Kimizuka, Y. Takeda, M. Takano, Phys. Rev. B 45 (1992) 1561–1570.
[3] H. Obayashi, Y. Sakurai, T. Gejo, J. Solid State Chem. 17 (1976) 299–303.
[4] S. Srinivasan, B.B. Dave, K.A. Murugesamoorthi, A. Parthasarathy, A.J. Appleby, in: L.J.M.J. Blomen, M.N. Migerwa (Eds.), Fuel Cell Systems, New York, 1999, p. 58.
[5] C.P. Khattak, F.F.Y. Wang, in: K.A. Gschneidner Jr., L. Eyring (Eds.), Handbook of the Physics and Chemistry of Rare Earths, North-Holland, Amsterdam, 1979, pp. 525–607.
[6] T. Katsura, T. Sekine, K. Kitayama, T. Sugihara, N. Kimizuka, N. J. Solid State Chem. 23 (1978) 43–57.
[7] N. Kimizuka, A. Yamamoto, H. Ohashi, T. Sugihara, T. Sekine, J. Solid State Chem. 49 (1983) 65–76.
[8] K. Saito, A. Sato, A. Bhattacharjee, M. Sorai, Solid State Commun. 120 (2001) 129–132.
[9] A. Bhattacharjee, K. Saito, M. Sorai, J. Phys. Chem. Solids 63 (2002) 569–574.
[10] K. Saito, Y. Yamamura, J. Mayer, H. Kobayashi, Y. Miyazaki, J. Ensling, P. Gutlich, B. Lesniewska, M. Sorai, J. Magn. Magn. Mat. 225 (2001) 381–388.
[11] A.B. Harris, H. Meyer, Phys. Rev. 127 (1962) 101–118.
[12] V.S. Varazashvilli, M.S. Tsarakhov, G.D. Chachanidze, Neorgan. Mater. 26 (1990) 602–604.
[13] S.C. Parida, S. Dash, Z. Singh, R. Prasad, V. Venugopal, J. Alloys Compnds. 280 (1998) 94–98.
[14] S.C. Parida, S. Dash, Z. Singh, R. Prasad, K.T. Jacob, V. Venugopal, J. Solid State Chem. 164 (2002) 527–534.
[15] S.C. Parida, K.T. Jacob, V. Venugopal, J. Phase Equilibria 25 (2003) 431–440.
[16] S.C. Parida, S.K. Rakshit, S. Dash, Z. Singh, R. Prasad, V. Venugopal, J. Solid State Chem. 172 (2003) 370–380.
[17] S.C. Parida, K.T. Jacob, V. Venugopal, Solid State Sci. 4 (2002) 1245–1255.
[18] S.K. Rakshit, S.C. Parida, S. Dash, Z. Singh, R. Prasad, V. Venugopal, J. Chem. Thermodynamics 35 (2003) 1793–1807.
[19] S.C. Parida, S.K. Rakshit, S. Dash, Z. Singh, R. Prasad, V. Venugopal, J. Chem. Thermodynamics 36 (2004) 911–917.
[20] S.K. Rakshit, S.C. Parida, S. Dash, Z. Singh, R. Prasad, V. Venugopal, Mat. Res. Bull. 40 (2005) 323–332.
[21] J.N. Pratt, Metall. Trans. A 21A (1990) 1223–1250.
[22] D.A. Shores, R.A. Rapp, J. Electrochem. Soc. 118 (1971) 1107–1111.
[23] M. Eibschutz, S. Shtrikman, D. Treves, Phys. Rev. 156 (1967) 562.
[24] S. Stølen, F. Grønvold, H. Brinks, T. Atake, H. Mori, J. Chem. Thermodynamics 30 (1998) 365–377.
[25] E.F. Westrum Jr., B.H. Justice, J. Phys. Chem. 67 (1963) 659–665.
[26] F. Gronvold, E.F. Westrum Jr., J. Am. Chem. Soc. 81 (1959) 1780–1783.
[27] F. Gronvold, E.J. Samuelsen, Phys. Chem. Solids 36 (1975) 249–256.
[28] E.J. Samuelsen, G. Shirane, Phys. Status Solidi 42 (1970) 241–256.
[29] W. Schnelle, R. Fischer, E. Gmelin, J. Phys. D: Apply. Phys. 34 (2001) 846–851.
[30] R. Pauthenet, J. Appl. Phys. 30 (1959) 290S–292S.
[31] A.J. Henderson Jr., D.G. Onn, H. Meyer, Phys. Rev. 185 (1969) 1218–1229.
[32] B. Mirianashvili, V.S. Varazashvili, M.S. Tsarakhov, T.A. Pavlenishvili, Russ. J. Inorg. Chem. 42 (1997) 926–928.
[33] V.S. Varazashvili, M.S. Tsarakhov, T.B. Mirianashvili, Russ. J. Inorg. Chem. 42 (1997) 597–599.
[34] R. Moretti, G. Ottonello, Geochim. Cosmochim. Acta 62 (1998) 1147–1173.
[35] I. Barin, Thermochemical Data of Pure Substances, vols. I & II, third ed., VCH Publishers, New York, 1995.
[36] B. Sundman, J. Phase Equilibria 12 (1991) 127–140.